

# **Analysis of a Tornadic Mesoscale Convective Vortex Based on Ensemble Kalman Filter Assimilation of CASA X-band and WSR-88D Radar Data**

Nathan Snook<sup>1,2</sup>, Ming Xue<sup>1,2</sup>, and Youngsun Jung<sup>2</sup>

School of Meteorology<sup>1</sup> and Center for Analysis and Prediction of Storms<sup>2</sup>  
University of Oklahoma, Norman OK 73072

Submitted to Monthly Weather Review

November 2010  
Revised April 8, 2011

Corresponding author address:  
Nathan Snook  
Center for Analysis and Prediction of Storms  
University of Oklahoma,  
120 David Boren Blvd, Room 5240, Norman OK 73072  
[nsnook@ou.edu](mailto:nsnook@ou.edu)

## Abstract

One of the goals of the National Science Foundation Engineering Research Center (ERC) for Collaborative Adaptive Sensing of the Atmosphere (CASA) is to improve storm-scale numerical weather prediction (NWP) by collecting data with dense X-band radar network which provides high-resolution low-level coverage, and by assimilating such data into NWP models. During the first spring storm season after the deployment of 4 radars in the CASA IP-1 (Integrated Project-1) network in southwest Oklahoma, a tornadic mesoscale convective system (MCS) was captured by CASA and surrounding WSR-88D radars on 8-9 May 2007. The MCS moved across northwest Texas and western and central Oklahoma; 2 tornadoes of EF-1 intensity and 1 tornado of EF-0 intensity were reported during the event, just to the north of the IP-1 network. This was the first tornadic convective system observed by CASA.

To quantify the impact of CASA radar data in storm-scale NWP, a set of data assimilation experiments were performed using the ARPS ensemble Kalman filter (EnKF) system configured with full model physics and high-resolution terrain. Data from 4 CASA IP-1 radars and 5 WSR-88D radars were assimilated in some of the experiments. The ensemble contained 40 members, and radar data were assimilated every 5 minutes for 1 hour. While the assimilation of WSR-88D data alone was able to produce a reasonably accurate analysis of the convective system, assimilating CASA data in addition to WSR-88D data is found to improve the representation of storm-scale circulations, particularly in the lowest few kilometers of the atmosphere, as evidenced by analyses of gust front position and comparison of simulated  $V_r$  with observations. Assimilating CASA data decreased RMS innovation of the resulting ensemble mean analyses of Z, particularly in early assimilation cycles, suggesting that the addition of CASA data allowed the EnKF system to more quickly achieve a good result. Use of multiple microphysics schemes

in the forecast ensemble was found to alleviate under-dispersion by increasing the ensemble spread. This work is the first assimilating real CASA data into an NWP model using EnKF.

## 1. Introduction

Accurate prediction of individual deep, moist convective storms is one of the major challenges of modern numerical weather prediction (NWP) in research and operational settings. Fully resolving all important storm-scale circulations is very expensive from a computational standpoint. In addition, most existing observing networks are quite sparse relative to the spatial scale of the flows being predicted, and offer incomplete observational coverage in both physical and parameter spaces. These challenges are then compounded by uncertainties and errors within NWP models. As computational power continues to increase, and as new high-resolution observing platforms, such as densely networked X-band radars (McLaughlin et al. 2009), are deployed to address the issues described above, a new challenge has arisen: assimilating data from multiple observing systems to best estimate the current state of the atmosphere and initialize storm-scale NWP models.

Because convective-scale errors generally grow very quickly (Lorenz 1969), it is vital to obtain the best possible estimate of the atmospheric state for NWP model initialization, ideally accompanied with an estimate of the uncertainty. While objective analysis can often be used for the purpose of obtaining a gridded analysis when observed and state variables are the same, remote sensing platforms such as radar and satellite do not directly observe most state variables, necessitating advanced data assimilation methods able to ‘retrieve’ state variables not directly observed. Such methods usually take advantage of physical laws linking various state variables and/or utilize information contained in observations taken at different times. They also try to obtain the ‘optimal’ state estimation by taking into account errors associated with various sources of information. Four-dimensional variational data assimilation (4DVAR) directly uses the numerical model to provide constraints among the estimated state variables, while the ensemble

Kalman filter (Evensen 1994) utilizes statistical correlations among variables derived from an ensemble of predictions to achieve a similar goal.

For convective-scale NWP, the only observing platform currently capable of providing spatially and temporally complete coverage of a convective system at a resolution sufficient to capture storm-scale features is Doppler radar. In the United States, the National Weather Service (NWS), together with other collaborating agencies, operates the WSR-88D radar network (Crum et al. 1993), consisting of 158 S-band Doppler radars with a maximum range of 248 nautical miles. While the WSR-88D network is relatively efficient at scanning the precipitating atmosphere, the long-range radars comprising the WSR-88D network cannot reach the lower troposphere beyond a limited distance from the radar site because of the curvature of the earth. Limited low-level radar coverage presents a problem for convective-scale data assimilation and NWP; many aspects of storm- and sub-storm-scale dynamics are sensitive to the near-surface atmospheric state, including the low-level cold pool and its interaction with the surrounding environment (e.g., Rotunno et al. 1988; Markowski et al. 2002; Snook and Xue 2008).

To address the near-surface observation problem described above, the Engineering Research Center (ERC) for Collaborative Adaptive Sensing of the Atmosphere (CASA) was established to develop short-range, networked X-band radars designed to be deployed in close proximity to one another (McLaughlin et al. 2009). The primary CASA testbed is located in southwest Oklahoma and consists of a network of four dual-polarized X-band radars with a maximum range of 40 km (Brotzge 2010b). This radar network is located roughly halfway between WSR-88D sites KTLX at Oklahoma City and KFDR at Frederick, OK; a location upstream of the Oklahoma City metropolitan area during prevailing westerly and southwesterly

flow during the warm season. At the network location, neither KTLX nor KFDR can sample the lowest kilometer of the atmosphere (Xue et al. 2006), maximizing the potential benefit of increased low-level coverage provided by the CASA radars. A comparison of the key specifications of CASA and WSR-88D radars is shown in Table 1. Despite having relatively wide beams compared to WSR-88D (Table 1), the CASA radars possess such advantages as a radial gate spacing of 100 m, a shorter mean range distance of observations (hence higher mean cross-beam resolutions), and a dynamic adaptive scanning strategy that identifies targets of meteorological interest and chooses an optimal combination of sector scans and full-circle scans at up to eight elevation angles to maximize the spatial and temporal coverage of features of greatest interest (Brotzge et al. 2005).

Commonly used methods for assimilating radar data into storm-scale NWP models include the three dimensional variational (3DVAR, e.g., Xue et al. 2003; Hu et al. 2006), and four-dimensional variational methods (4DVAR, e.g., Sun et al. 1991; Sun and Crook 1997, 1998), and EnKF (e.g., Snyder and Zhang 2003; Dowell et al. 2004a; Tong and Xue 2005b). Compared to 3DVAR, EnKF has the notable advantage of being able to incorporate multivariate, flow-dependent error covariance, including cross-covariance, as derived from the ensemble (Evensen 2003), allowing effective ‘retrievals’ of state variables from radial velocity and radar reflectivity (Snyder and Zhang 2003; Tong and Xue 2005b). Unlike 4DVAR, EnKF does not require the development of an adjoint model; such development is labor intensive and the resulting adjoint model often has difficulties with highly nonlinear processes. In addition, ensemble forecasts are believed to be particularly important for storm-scale NWP (Xue et al. 2007). EnKF naturally provides a set of analyses that in principle best characterizes the analysis uncertainty; such analyses can therefore serve as initial conditions for ensemble forecasts.

One of the important goals for the CASA project is to evaluate the value and benefit of data collected by its experimental testbed radars. Preliminary results using the ARPS (Xue et al. 2000; Xue et al. 2003) Data Analysis System (ADAS, Brewster 1996), together with its cloud analysis package, for data assimilation (Brewster et al. 2007) show a generally positive impact from the addition of IP1 data. On 8-9 May 2007, a mesoscale convective system (MCS) with a pronounced line-end vortex (LEV) developed over southwestern Oklahoma and produced several tornadoes shortly after moving out of the CASA domain. Schenkman et al. (2010) studied this case, using ARPS 3DVAR and a cloud analysis to assimilate CASA and WSR-88D reflectivity and radial velocity data, and demonstrated positive impact of CASA IP1 data on the prediction of the MCS. In this study, we apply the ARPS EnKF system (Tong and Xue 2005; Xue et al. 2006) to the 8-9 May 2007 LEV event and further evaluate the impact of CASA radar data.

EnKF has proven to be very effective in retrieving accurate and dynamically consistent wind, temperature, and microphysical fields from reflectivity and radial velocity observations when using simulated observations (e.g., Snyder and Zhang 2003; Zhang et al. 2004; Tong and Xue 2005a; Xue et al. 2006; Tong and Xue 2008b). Obtaining analyses that lead to good short-range forecasts of convective storms, however, remains a challenge (Dowell et al. 2004b; Tong 2006); most storm-scale EnKF studies to date have focused on analysis rather than forecasting; thus relatively few papers showing good forecast results have been published so far, except for Lei et al. (2009) and Dowell et al. (2010). This study investigates the ability of a storm-scale EnKF system to produce a quality analysis by assimilating radial velocity and reflectivity data from four X-band CASA IP1 radars and five S-band WSR-88D radars during CASA's first observed tornadic system. Forecast results will be addressed in a future paper.

CASA also seeks to detect, track, analyze, and predict tornadoes or processes leading to

tornadogenesis (McLaughlin et al. 2009). Most previous studies involving analysis or simulation of tornadic storms have focused on supercells (e.g., Klemp et al. 1981; Klemp and Rotunno 1983; Rotunno 1993; Dowell and Bluestein 1997; Dowell et al. 2004a). While not as common as tornadoes within supercells, non-supercellular tornadoes make up a significant portion of tornado occurrences. Trapp et al. (2005) found evidence suggesting that approximately 20% of tornadoes within the continental United States are not associated with cellular convection, and that most tornadoes from non-cellular convection occur in association with bow echoes, or LEVs (e.g., Weisman 1993) within an MCS, as was the case on 8-9 May 2007.

This study addresses two major goals: (1) developing and demonstrating the ability of an EnKF method in assimilating real data from radars with different operating characteristics (including S-band WSR-88D radars with 360 degree scans and X-band CASA radars with sector scans) to accurately estimate the state of a mesoscale convective system; and (2) assessing the added value of CASA radar data in the resulting analyses. The remainder of this paper is organized as follows: Section 2 describes the details of the 8-9 May 2007 MCS case, the radar data used and their pre-processing, the numerical model used, and the EnKF data assimilation method and procedure. In section 3, results of the EnKF analysis are presented and analyzed. Section 4 contains further discussion, summary, and conclusions.

## **2. Case, Data, and Methods**

In this study, we apply a version of the ARPS EnKF data assimilation system (Tong and Xue 2005b; Xue et al. 2006; Tong and Xue 2008a), modified to allow the use of mixed-microphysics ensembles, to assimilate the CASA and WSR-88D radar data gathered on 8-9 May 2007 during the first tornadic case observed by the CASA IP-1 radar network. During this

event, a MCS with a pronounced LEV developed and moved through much of southwest/central Oklahoma and passed directly over the CASA IP1 network. This system spawned two confirmed EF-1 tornadoes and one confirmed EF-0 tornado in central Oklahoma between 0354 UTC and 0443 UTC, just north of the IP-1 network.

*a. 8-9 May 2007 case overview*

The location, timing, and intensity of the three tornadoes that developed during the evening of 8 May 2007 are summarized in Fig. 1. Among the two EF1 tornadoes, the first occurred near Minco, OK at 0354 UTC, 9 May 2007, and the second occurred near El Reno, OK at 0443 UTC. The third, weaker, EF-0 tornado was confirmed near Union City, OK, reported at 0426 UTC. The El Reno tornado was the most destructive of the three, causing an estimated \$3 million of damage. Of these three tornadoes, only for the El Reno tornado did the NWS issue a tornado warning prior to tornado occurrence, underscoring the challenge of forecasting tornadoes within MCSs.

During the afternoon and evening of 8 May 2007, a surface low was developing in southwest Oklahoma near the intersection of a nearly stationary east-west frontal boundary and an advancing cold front to the west (not shown). Multicellular convection along the cold front grew into a MCS (Kumjian and Ryzhkov 2008) beginning around 1200 UTC on 8 May 2007, in an area of upper-level divergence associated with a cyclonically curved jet streak. The MCS continued to grow in coverage, and by 0000 UTC on 9 May 2007 extended over much of central and north Texas and southwestern Oklahoma and featured a surging bow echo located along its leading edge (Fig. 2a). While the portion of the MCS in Texas began to weaken after 0100 UTC, the northern portion of the system persisted until approximately 0730 UTC (Fig. 2b-f).

Strong low-level rotation was observed in the system as early as 0021 UTC and a brief tornado was reported by local media west of Lake Elsworth, OK, at 0115 UTC; however, a subsequent damage survey was unable to confirm this report (Brotzge 2009), and no further tornadic activity was reported until 0354 UTC.

Beginning approximately 2200 UTC on 8 May, a LEV formed near the northern end of the bow echo, just south of the Red River in northwest Texas. The development of the LEV occurred as the MCS merged with a supercell to its northeast (Schenkman et al. 2010). The LEV moved north-northeast and contracted as it moved into southwestern Oklahoma (Brotzge 2010a). The LEV intensified between 0230 and 0300 UTC as it interacted with and absorbed a supercell in Comanche County OK (Fig. 2b,c); evidence of this intensification was present in both WSR-88D radar reflectivity and mesonet observations (Schenkman et al. 2010) . The LEV reached its peak intensity between 0330 and 0530 UTC (Fig. 2e,f), during which time all three reported tornadoes occurred. Observations from the Oklahoma mesonet indicate that at its peak, the LEV contained a well-defined surface circulation with approximately  $25 \text{ ms}^{-1}$  of horizontal wind shear (Schenkman et al. 2010). The observed evolution of the MCS and its associated LEV closely fits the conceptual model presented in Fujita (1978), as well as the conceptual model of an asymmetric convective system presented by Houze et al. (1989).

#### *b. Model configuration and experiment setup*

In this study, a  $259 \times 259 \times 43$  ARPS grid with 2 km horizontal spacing is used for analyses and forecasts; vertical grid stretching is applied, giving a near-surface vertical grid spacing of approximately 100 m. The model top is at a height of 20 km. Full model physics

are used (Xue et al. 2001), including the NASA Goddard Space Flight Center long- and shortwave radiation parameterization, a two-layer soil model, surface fluxes parameterized using predicted surface temperature and water content, and a 1.5-order turbulent kinetic energy (TKE)-based subgrid-scale turbulence parameterization, along with high-resolution terrain. A one-hour-long pre-forecast is performed before EnKF data assimilation cycles begin, initialized from the 9 May 2007 NCEP 0000 UTC NAM analysis. At 0100 UTC, smoothed random perturbations are added to the 1-hour forecast using the method of Tong and Xue (2008b) to create a set of initial conditions from which ensemble forecasts are launched. The smoothed perturbations with a horizontal length scale of 8 km and a vertical length scale of 5 km are added to the horizontal wind field with a standard deviation of  $2 \text{ m s}^{-1}$ , to the mixing ratios of hydrometeors, cloud water, and cloud ice with a standard deviation of  $0.001 \text{ kg kg}^{-1}$ , and to the potential temperature field using positive perturbations only with a standard deviation of 2 K. The EnKF algorithm used is the ensemble square-root filter (EnSRF) of Whitaker and Hamill (2002). Radar data are assimilated every 5 minutes from 0100 to 0200 UTC. The observation error standard deviations are assumed to be  $1 \text{ m s}^{-1}$  for radial velocity and 2 dBZ for radar reflectivity. The observation operator used to map the model state to observation space for radar reflectivity and radial velocity follows that of Jung et al. (2008). To sample radar data on the radar elevation angles, a Gaussian power-gain function following Wood and Brown (1997) is used as in Xue et al. (2006). The covariance localization radius is set to 6 km. Lateral boundary conditions are provided by the NCEP NAM 6-hourly analyses and intervening 3 hour forecasts. This setup is summarized in Fig. 3; forecast results from 0200 to 0500 UTC (Fig. 3) will be the subject of a future paper.

Results from three experiments are reported here: a control experiment (hereafter referred

to as “CNTL”) using a mixture of three microphysics schemes (described below) in the forecast ensemble and assimilating both WSR-88D and CASA data; an experiment using a mixed-microphysics ensemble and WSR-88D data only (hereafter “NoCASA”); and an experiment assimilating both WSR-88D and CASA data using a single- rather than mixed-microphysics ensemble (hereafter “NoMMP”). NoCASA is run to evaluate the impact of including CASA data in the analysis procedure, while NoMMP is run to examine the ability of a mixed-microphysics ensemble in reducing the under-dispersion of the ensemble. Fujita et al. (2007) found that the use of multiple physics parameterization schemes in their mesoscale EnKF system improved the resulting analysis of mesoscale features, and Meng and Zhang (2007) also reported that using a mixed-microphysics ensemble positively impacted their mesoscale analyses. However, these previous studies were not at a convection-resolving resolution and did not include radar. The differences in ensemble setup between experiments CNTL, NoCASA, and NoMMP are summarized in Table 2.

In all experiments, 5-minute interval level-II volume scans of WSR-88D radial velocity and reflectivity from five WSR-88D radars are assimilated: they include radars at Oklahoma City, OK (KTLX), Vance Air Force Base, OK (KVNX), Amarillo, TX (KAMA), Dyess Air Force Base, TX (KDYX), and Lubbock, TX (KLBB). In experiments using CASA data, aggregate volumes of radial velocity and reflectivity data are assimilated, also at 5 minute intervals, from each of the four CASA IP-1 radars: Cyril, OK (KCYR); Lawton, OK (KLWE); Rush Springs, OK (KRSP); and Chickasha, OK (KSAO). Aggregate CASA radar volumes are created by first interpolating raw CASA sector scan data on observed elevations to a uniform radial grid with azimuthal spacing of 1 degree, and then interpolating in time to the center of a five-minute window valid at the assimilation time. For each radial, the nearest data before and after the

assimilation time within the five-minute window are linearly interpolated in time to obtain the corresponding radial in the aggregate volume scan. If only one scan is available for a given radial, that scan is used. If no scans are available, that radial is marked as missing.

A summary of the radars used and their locations is provided in Table 3. The WSR-88D radar sites used were selected to provide the best coverage of the MCS; Frederick Air Force Base, OK (KFDR) is excluded because its level-II data are unavailable during the assimilation period. WSR-88D radar data underwent automated quality control during preprocessing to eliminate noise and ground clutter, and perform despeckling and velocity de-aliasing (Brewster et al. 2005). CASA radar data were subject to automated quality control during signal processing, including filtering of ground clutter, velocity de-aliasing, and range overlay suppression (Bharadwaj et al. 2010). No additional quality control was performed on CASA data during interpolation. We point out here that while some previous convective-scale EnKF studies have used real radar data (e.g., Tong 2006; Aksoy et al. 2009; Dowell and Wicker 2009; Aksoy et al. 2010), and some have used full terrain and model physics (e.g., Tong 2006; Meng and Zhang 2008; Stensrud and Gao 2009), to the authors' knowledge, this is the first study to assimilate real radar reflectivity and radial velocity observations from multiple radar networks (WSR-88D and CASA) using full terrain and model physics.

In order to counteract the inherent tendency of the ensemble to converge to a solution different from the true state of the atmosphere, a method for maintaining ensemble spread is needed (Anderson and Anderson 1999; Dowell and Wicker 2009). To this end, a multiplicative covariance inflation (Anderson and Anderson 1999; Tong and Xue 2005b) factor of  $\gamma = 1.25$  is applied to the prior ensemble; this value was found to be large enough to maintain the ensemble

spread, but not so large as to cause numerical instability in the model time integration (a problem which occurred in tests using too large an inflation factor). In recent work, other techniques have been applied to increase ensemble spread—for example, Zhang et al. (2004) used a “relaxation” technique, restoring a pre-set fraction of ensemble spread reduced by the filter correction. Random additive perturbations to various model fields have also been employed; Dowell and Wicker (2009) found that applying smoothed additive perturbations to the horizontal wind, potential temperature, and water vapor fields yielded a significant increase in the resulting ensemble spread. Additive errors were tried in our earlier experiments without significant improvement to our results and are hence not used here. It is likely that proper scaling may be needed and an optimal combination with multiplicative inflation may exist, which will be a subject for future studies.

Because of the strong reflectivity attenuation inherent to X-band radar data in areas of heavy precipitation, attenuation correction using polarimetric differential phase (Chandrasekar et al. 2004) was applied to CASA data before they were used. Accurate attenuation correction is vital; if uncorrected, attenuated radar data were assimilated, the erroneously low values of reflectivity in the attenuated regions would negatively impact the analysis. While the attenuation correction algorithm used has been shown to accurately retrieve un-attenuated reflectivity values (Chandrasekar et al. 2004), it can only do so when the reflected power is above the noise floor of the radar receiver. When total attenuation occurs, the resulting radar data cannot be objectively distinguished from true clear-air data; these areas of total attenuation appear as “shadows” of near-zero reflectivity in areas which may actually contain significant precipitation. To avoid erroneous assimilation of completely attenuated reflectivity data, CASA reflectivity and radial velocity data were assimilated only in regions where attenuation-corrected reflectivity exceeded

20 dBZ. Unfortunately, this constraint eliminates the ability of CASA reflectivity data to suppress spurious storms that occur in regions free of observed reflectivity; Tong and Xue (2005) showed that the assimilation of reflectivity data in non-precipitation regions is very beneficial in suppressing spurious storms. Furthermore, though CASA data were not assimilated when attenuation-corrected reflectivity was less than 20 dBZ, because no reliable way exists to objectively distinguish fully-attenuated regions from clear air echo regions, attenuated areas were included in the RMS innovation computation at CASA sites, resulting in increased RMS innovation values for the CASA radars. Finding new ways to more effectively use X-band reflectivity data remains an important research topic (Xue et al. 2009).

As in Xue et al (2006), a 40 member ensemble is used. For CNTL and NoCASA, three different single-moment ice microphysics schemes are used in the ensemble. The schemes used are an implementation of the three-ice scheme of Lin et al. (1983) with modifications following Tao and Simpson (1993), an ARPS implementation of the Weather Research and Forecasting (WRF) model single-moment 6-class microphysics (WSM6) scheme (Hong and Lim 2006), and the simplified NWP explicit microphysics (NEM) scheme of Schultz (1995). In CNTL and NoCASA, 16 members use the Lin scheme, 16 use the WSM6 scheme, and 8 use the NEM scheme. In NoMMP, all 40 ensemble members employ the Lin microphysical scheme.

### **3. Results and analysis**

By the end of the assimilation period at 0200 UTC 9 May 2007, all three experiments produce a MCS with reflectivity structure very similar to that observed by radar. Composite radar data calculated from model fields for CNTL, NoCASA, and NoMMP (Fig. 4a-c) correspond well to composite radar reflectivity measured by WSR-88D (Fig. 4d). Analyzed

composite reflectivity at 0200 UTC for all three experiments compares closely with observed reflectivity in terms of the intensity and location of the main convective cells and stratiform rain region and the overall shape of the bow echo (Fig. 4). In both model simulations and observations, a LEV is present at the northern end of the line of strongest convection, located in the western portion of the CASA IP1 network (Fig. 4). Subtle differences between experiments are present in the composite reflectivity fields near the CASA network (Fig. 4a-c). Minor differences between the analyses (Fig. 4a-c) and the observations (Fig. 4d) of radar reflectivity are notable in the southern portion of the domain, where all three experiments underestimate the coverage and intensity of the strong echo region where the reflectivity is greater than 35 dBZ. Insufficient low-level radar coverage in southwestern portion of the domain is believed to have contributed to the model error there, while underestimation of the intensity of the main convective line is likely due to under-correction to the background forecast by the ensemble filter, which can occur as a result of under-dispersion in the ensemble.

Despite the overall qualitative similarity in analyzed reflectivity (Fig. 4), important differences between the three experiments exist throughout the assimilation period. Both the inclusion of CASA data and the use of a mixed-microphysics ensemble produce notable differences in the forecast and analysis states during the assimilation cycles. We will examine these aspects in turn, beginning with the impact of additional CASA radar data.

#### *a. Impact of assimilating CASA data*

CASA seeks to improve storm-scale analyses and forecasts by sampling the near-surface flow at high resolution. Experiment NoCASA is designed to evaluate the impact of withholding CASA data during assimilation. While CNTL and NoCASA produce qualitatively

similar reflectivity fields (Fig. 5), the impact of assimilating CASA data can be seen in horizontal wind fields of CNTL and NoCASA, particularly in lower levels of the atmosphere (Fig. 5); strong southerly and southeasterly flow is present at one kilometer above mean sea level (approximately 700 m above the surface) within the northern portion of the leading convective line in CNTL (located in the region shared by the two western CASA radars, Fig. 5a), while the corresponding flow in NoCASA is much weaker (Fig. 5c). In addition, in experiments assimilating CASA data (Fig. 5a, b), in the southern portion of the CASA domain, southwest winds are present within and just ahead the convective line just to the south of the notch in the line near the southwestern-most CASA radar (KLWE). By contrast, this notch is less noticeable in NoCASA (Fig. 5c), and the low-level winds in the region are from the southeast. These differences represent the accumulated effects of assimilating CASA data. This result agrees well with results reported by Schenkman et al. (2010), who found that assimilation of CASA  $V_r$  data for this case using a 3DVAR and cloud analysis package had a strong impact on low-level winds and gust front structure.

The assimilation of CASA data results in a marked increase in maximum vertical vorticity in the lowest several kilometers of the atmosphere that sets the stage for tornadic processes. Fig. 6 shows the time-height cross-section of maximum vertical vorticity within a box tightly surrounding the CASA domain (depicted in Fig. 2a), for experiments CNTL and NoCASA. In CNTL, where CASA data were assimilated, much higher maximum values of low-level vertical vorticity are consistently present within this domain in both the forecast priors and EnKF analyses as compared to NoCASA. In particular, strong vertical vorticity is present in CNTL between 5100 and 6600 s of forecast time (0125 to 0150 UTC) between the surface and the 3 km level; a much weaker maximum is also present in NoCASA, but it is not discernible

until 5400 s (0130 UTC).

Between 0125 and 0150 UTC, a strong low-level circulation is present west-southwest of KTLX, within the CASA domain. This circulation is visible in CASA and WSR-88D radar observations between 0120 and 0150 UTC, but is much better resolved by CASA radars due in large part to shorter range (not shown). The NWS Norman forecast office issued a tornado warning for the storm cell containing this circulation at 0126 UTC, although a later storm survey found no evidence of an actual tornado at this particular time and location. Inclusion of CASA data resulted in the analysis of a stronger low-level rotation within the CASA domain, matching more closely with the observed evolution of the MCS. In CNTL, where CASA data were assimilated, this circulation is present throughout the time it was observed by radar (Fig. 6a); by contrast, NoCASA is slower in developing such a circulation and the resulting low-level vertical vorticity is weaker (Fig. 6c).

The tornado-warned meso-vortex is well-observed by CASA radar KCYR. The  $2^{\circ}$  elevation  $V_r$  observations from KCYR at 0140 UTC (Fig. 7a) show a strong circulation present between 5 and 20 km to the west of the radar site, with  $45 \text{ m s}^{-1}$  of horizontal wind shear over a distance of approximately 12 km. Simulated KCYR  $V_r$  observations from the 0140 UTC ensemble mean analysis of CNTL (Fig. 7b) also indicate the presence of a meso-vortex circulation which closely matches the location and size of that seen in the KCYR observations, but with a slightly weaker maximum horizontal shear of around  $40 \text{ m s}^{-1}$  across the vortex. Simulated KCYR  $V_r$  observations from NoCASA (Fig. 7c) show no strong circulation at the  $2^{\circ}$  elevation; instead, a convergent signature with only very weak rotation is present near the location of the observed meso-vortex. In addition, NoCASA (Fig. 7c) greatly underestimates the region of positive  $V_r$  observed to the northwest of KCYR (Fig. 7a); by contrast, the ensemble

mean analysis of CNTL (Fig. 7b) indicates a flow that closely matches KCYR observations. These results highlight the importance of assimilated near-surface CASA radar data in accurately capturing the near-surface flow in this convective system.

The impact of assimilated CASA data is also evident in the surface wind field and cold pool structure in the 0140 UTC analysis. In experiment CNTL (Fig. 8a), a moderately intense surface circulation is present, horizontally co-located with that indicated by KCYR  $V_r$  observations. In the CNTL analysis, a moderately strong gust front is present to the south and southeast of the surface circulation, with strong inflow of between 15 and 25  $\text{ms}^{-1}$  ahead of the gust front. The location of the gust front in the 0140 UTC CNTL analysis (Fig. 8a) is similar to that indicated by the full-resolution 0139 UTC KCYR  $2^\circ V_r$  observations (Fig. 8c); at the location of the meso-vortex, these observations were 500 to 700 m above the surface. The surface wind field in the 0140 UTC ensemble mean analysis of NoCASA shows only weak rotation within a convergent shear zone (Fig. 8b), consistent with the simulated  $V_r$  observations of Fig. 7c. While the gust front present in NoCASA is positioned similarly to that in CNTL, it is much weaker, with a cross-frontal temperature difference of less than 2 K; this is too weak compared to potential temperature decreases of 3 to 4 K as measured by nearby Oklahoma Mesonet stations during passage of the gust front (not shown).

The stronger low-level circulation of CNTL is accompanied by more vigorous convective updrafts over the CASA subdomain. Total updraft flux is calculated at each model level over the CASA subdomain outlined in Fig. 2a; the resulting vertical profiles of updraft flux for the CNTL and NoCASA 0140 UTC ensemble mean analyses are plotted in Fig. 9a. Greater updraft flux is present in CNTL than in NoCASA, particularly below the 5 km level. Much of the difference in updraft flux between CNTL and NoCASA can be attributed to greater updraft

velocities in CNTL; histograms of updraft velocity for the 0140 UTC analyses of CNTL (Fig. 9b) and NoCASA (Fig. 9c) in model grid cells where the vertical velocity was greater than or equal to  $4 \text{ m s}^{-1}$  indicate that more regions of strong updrafts are present in CNTL than in NoCASA. In the 0140 UTC CNTL analysis, updrafts in excess of  $16 \text{ m s}^{-1}$  are present in more than 100 grid cells; the maximum updraft velocity observed within the CASA subdomain exceeds  $24 \text{ m s}^{-1}$ . In NoCASA, only about 30 grid cells have updrafts exceeding  $16 \text{ m s}^{-1}$ , and the maximum updraft velocity within the CASA domain is less than  $19 \text{ m s}^{-1}$ . Similar behavior was noted at other analysis times and during the forecast cycles, with stronger updrafts and greater updraft fluxes present in CNTL than in NoCASA (not shown).

#### *b. Innovation statistics during the EnKF analysis cycles*

To more quantitatively assess the behavior of the EnKF analyses, average root-mean-square (RMS) values of observation innovation (the difference between observations and the model state in the form of observed quantities) and ensemble spread are examined. Observation innovations and ensemble spread are calculated for each of the 4 CASA radars, as well as WSR-88D radars KTLX and KVN, for radar reflectivity ( $Z$ ) (Fig. 10) and radial velocity ( $V_r$ ) (Fig. 11), in experiments CNTL and NoCASA. Innovations in Fig. 10 and Fig. 11 are calculated for the ensemble mean fields at locations where either observed or model reflectivity is greater than or equal to 15 dBZ. The calculation is further limited to within the CASA subdomain (c.f., Fig. 2a). In NoCASA, RMS innovations for the CASA radars are calculated against CASA data that were not assimilated; these observations are therefore from independent sources. Nevertheless, EnKF data assimilation in NoCASA was able to decrease the average innovations at all CASA sites for  $Z$  during every assimilation cycle, and for  $V_r$  during almost every assimilation cycle

(Fig. 10, Fig. 11). Given that different radars measure different components of the velocity field, the reduction in innovation against independent, unassimilated radial velocity measurements indicates good performance of the EnKF.

Assimilation of CASA data resulted in a slight but notable decrease in RMS innovation in the analysis of  $Z$  in CNTL as compared to NoCASA (Fig. 11). The overall decrease was greater for the CASA radars, due to the absence of CASA data in NoCASA. Among the WSR-88D radars, only KTLX and KVNX are included for the comparisons between CNTL and NoCASA in Fig. 10-12 because they are located close to the center of the convective system during the assimilation period and share the greatest overlap with the CASA domain. The RMS innovations of  $V_r$  at KTLX and KVNX differ little between CNTL and NoCASA (Fig. 10a, b), though the RMS innovation of the CNTL analysis is very slightly lower than that of NoCASA at KTLX during early assimilation cycles (Fig. 10a). In contrast, a larger improvement is seen in  $Z$  for CNTL during early cycles for KTLX and early to middle cycles for KVNX as compared to NoCASA (Fig. 11). These results suggest that the inclusion of CASA data modestly improved the analyzed reflectivity field within the model, particularly during early assimilation cycles, with less improvement to the analysis of radial velocity.

For the WSR-88D sites (KTLX and KVNX), the greatest differences in RMS innovations of  $Z$  and  $V_r$  between CNTL and NoCASA occurred in the first six assimilation cycles (Fig. 10a, b; Fig. 11a, b). In addition, fewer cycles were needed for the analysis to reach its minimum RMS innovation value for  $Z$  in CNTL than in NoCASA. While the minimum RMS innovation of the analysis for  $Z$  was not reached until around the 8th assimilation cycle at KTLX (Fig. 11a) and the 11th assimilation cycle for KVNX (Fig. 11b) in NoCASA, the RMS innovation of the analysis reached its minimum value for these radars in CNTL by the 4th and 3rd cycles

respectively (Fig. 11a, b). Assimilation of CASA data reduces the number of cycles needed for the EnKF analysis to reach a relatively stable and low level of RMS innovation in  $Z$ .

One important measure of the performance of an EnKF data assimilation system is statistical consistency, as discussed in Snyder and Zhang (2003) and Dowell et al. (2004a). For forecasts and observations with independent error characteristics, the variance of the innovation should be equal to the sum of the observation and forecast error variances:

$$\sigma_d^2 = \sigma_o^2 + \sigma_f^2 \quad (1)$$

Following Dowell et al. (2004a), we arrive from (1) at a consistency relation valid for observations  $y^o$  and model forecast state  $x^f$ , with angle brackets representing an average over all available observations at a time, and overbars denoting an ensemble mean:

$$\frac{\sigma_o^2 + \left\langle \frac{1}{N-1} \sum_{i=1}^N \left[ H(x_i^f) - \overline{H(x^f)} \right]^2 \right\rangle}{\left\langle \left[ \left( y^o - \overline{H(x^f)} \right) - \left\langle \left( y^o - \overline{H(x^f)} \right) \right\rangle \right]^2 \right\rangle} \approx 1 \quad (2)$$

Here,  $N$  is the ensemble size,  $i$  is the ensemble index, and  $H$  is the observation operator. In practice, values of consistency ratio well below 1 are often seen in EnKF studies (e.g., Dowell et al. 2004b), indicating a general tendency for under-dispersion in the ensemble.

Time series of consistency ratio for CNTL and NoCASA, calculated during the assimilation period for four CASA and two WSR-88D (KTLX and KVN) radars are shown in Fig. 12. Values of consistency ratio for  $V_r$  and  $Z$  in both CNTL and NoCASA fall below the optimal value of approximately 1 throughout much of the period (Fig. 12) with the exception being for  $Z$  in early cycles at the WSR-88D radar sites (Fig. 12a, b) and CASA sites KRSP and KSAO (Fig. 12e, f). Consistency ratio for  $Z$  was much higher at the WSR-88D radar sites than

at CASA sites in both CNTL and NoCASA. Lower values of consistency ratio were observed for  $V_r$  than for  $Z$ , with  $V_r$  consistency ratio values of between 0.1 and 0.3 common for the CASA radars; WSR-88D sites KTLX and KVNX yielded  $V_r$  consistency ratios ranging from 0.2 to 0.3. Consistency ratios for  $Z$  were higher, ranging between 0.5 and 1.0 for WSR-88D radars, and 0.2 and 1.0 for CASA radars. Very high values (greater than 2.0) of consistency ratio for  $Z$  were present during the first few assimilation cycles due to the very high values of RMS ensemble spread for  $Z$  at these times (see Fig. 12).

Values of consistency ratio in experiments NoCASA and CNTL are slightly lower than those seen in previous real data studies using a similar EnKF setup, such as Dowell et al. (2004b). One can infer from the particularly low values of consistency ratio seen for  $V_r$  (Fig. 12) that a significant amount of under-dispersion exists in the radial velocity field in both NoCASA and CNTL. In this study, we assumed an observation error standard deviation of 1 m s<sup>-1</sup> for radial velocity observations. The relatively small assumed observation error may be a contributing factor in the low values of consistency ratio observed. In future studies, we will consider increasing the assumed observation error to 2 m s<sup>-1</sup> for  $V_r$ . Values of consistency ratio for  $Z$  are also below 1, suggesting insufficient ensemble spread in the reflectivity field, but this deficiency is not as severe as that in the radial velocity field. Dowell et al. (2009) addressed under-dispersion in radial velocity by using additive perturbations to the horizontal wind field; however, initial tests for this case including additive perturbations to the wind field did not show improvement in RMS innovation for radar reflectivity and radial velocity observations when compared against analyses using multiplicative covariance inflation alone; further tests using perturbations with different perturbation magnitudes and scales will be explored in future work on this case.

The difference in the consistency ratio time series (Fig. 12) between CASA and NoCASA for Z (and to a lesser extent  $V_r$ ) indicates that the under-dispersion is slightly less severe in CNTL than in NoCASA, particularly during early assimilation cycles and at the WSR-88D radar sites (Fig. 12a, b). Assimilation of CASA data slightly decreases under-dispersion of radar reflectivity within the ensemble; this is a somewhat counter-intuitive result, as increasing the amount of data assimilated usually results in decreased spread within the ensemble. This is likely to be due to the way that initial perturbations are added. In this study, initial perturbations were only added to grid points within 2 km in the horizontal and 1 km in the vertical of observed radar reflectivity exceeding a threshold of 5 dBZ, following the methodology of Tong and Xue (2005). Because CNTL includes CASA data in addition to WSR-88D radar data, the region containing initial perturbations is slightly larger in CNTL than in NoCASA, particularly at low-levels where only CASA radar data is available. Accordingly, the initial difference in RMS spread is greater for CASA radars and very small for WSR-88D radars (Fig. 10). The effect of this slight difference in the initial perturbation region fades as assimilation cycles are performed; by the end of the assimilation window CNTL shows smaller spread in the later cycles due to faster spread reduction, as expected when assimilating more observations.

### *c. Impact of using a mixed-microphysics ensemble*

In previous studies, using different parameterization schemes among ensemble members (e.g., Meng and Zhang 2007) and including perturbations of microphysical parameters within the ensemble (e.g., Ge et al. 2010) have been shown effective in increasing ensemble spread and reducing under-dispersion within the ensemble. However, the use of multiple microphysics schemes for real-case storm-scale radar data assimilation has, to our knowledge, not been

reported in the literature. In this section, different microphysics schemes are used among ensemble members and the effect on the analysis is investigated. Experiment NoMMP was performed to evaluate the effect of using a mixed-microphysics ensemble; NoMMP differed from CNTL only in that it used Lin microphysics for all members in the ensemble forecast (see Table 2).

Time-series of RMS innovation and spread during assimilation for experiments CNTL and NoMMP are presented in Fig. 13 for  $V_r$  and Fig. 14 for Z. Since the impact of the mixed-microphysics ensemble is present throughout the model domain, RMS spread and innovation calculations were not limited to the CASA subdomain (see Fig. 2a) for comparisons between CNTL and NoMMP. Thus, unlike in the comparison between CNTL and NoCASA, calculations are presented for all five WSR-88D radars in addition to the four CASA radars; data from all these radar sites were assimilated in both CNTL and NoMMP.

The impact of the mixed-microphysics ensemble on RMS innovation of  $V_r$  (Fig. 13) is relatively small. The RMS innovation of the  $V_r$  analysis of CNTL is slightly lower than that of NoMMP at KTLX during the first five assimilation cycles (Fig. 13d); however farther to the west at radar site KAMA (Fig. 13a), NoMMP actually produces a slightly lower RMS innovation for  $V_r$  during later cycles of the assimilation period. At most sites no significant difference in RMS innovation of  $V_r$  can be seen. Likewise, RMS ensemble spread of  $V_r$  is virtually unchanged between CNTL and NoMMP.

In contrast to  $V_r$ , differences between the RMS innovation and ensemble spread of Z in NoMMP and CNTL (Fig. 14) are much more prominent. Compared to NoMMP, ensemble spread of Z in CNTL grows faster during the forecast step and remains higher during the analysis step; greater ensemble spread is consistently present in CNTL during forecasts and analyses than

in NoMMP at every radar site. Average RMS ensemble spread of  $Z$  during the forecast step decreases in the first several cycles and remains largely constant during the remainder of the assimilation period. Average RMS ensemble spread values for  $Z$  at the end of assimilation period range between about 3 to 5 dBZ in CNTL and between 1 and 4 dBZ in NoMMP.

Differences in the RMS innovation values of  $Z$  between CNTL and NoMMP (Fig. 14) are also noticeable but not as prominent as differences in RMS ensemble spread. Error in the forecast ensemble grows more quickly in CNTL than in NoMMP, evidenced by a steeper increase between each analysis and the subsequent forecast at every WSR-88D radar site, as members using different microphysics schemes arrive at varying solutions because of differences in treatment of microphysics processes. The faster growth of RMS innovation in CNTL (Fig. 14) can be attributed in part to variation in reflectivity formulation between the Lin, WSM, and NEM microphysical schemes—for this case, the NEM microphysics scheme greatly underpredicts the coverage of stratiform rain, thus members using the NEM microphysics scheme within the CNTL ensemble act to increase the RMS innovation during the forecast cycles. When innovation statistics for  $Z$  were derived for subsets of CNTL members using individual microphysical schemes, the subset consisting of NEM members within CNTL had the most rapid increase in RMS innovation of  $Z$  during forecast steps, while the subset consisting of Lin members within CNTL had the slowest increase (not shown). However, despite the higher RMS innovation values of  $Z$  present during the forecast step in CNTL, the RMS innovation of the analysis of  $Z$  in CNTL is equal to or lower than that of NoMMP for almost every analysis cycle at all radar sites. The greatest differences can be seen at KAMA and KVNX, where CNTL produces analyses of  $Z$  with an average RMS innovation of between 0.3 and 1 dBZ lower than corresponding analyses in NoMMP for most of the assimilation period. At the CASA

radar sites differences between CNTL and NoMMP are more difficult to discern; at these sites the two experiments produced qualitatively similar RMS innovation and ensemble spread time series.

Comparison of consistency ratio calculated for  $V_r$  and  $Z$  for experiments CNTL and NoMMP (Fig. 15) reveal that use of the mixed-microphysics ensemble results in a higher consistency ratio than the single-microphysics ensemble for  $Z$  because of increased ensemble spread of radar reflectivity in the mixed-microphysics case. In both CNTL and NoMMP the consistency ratio of  $V_r$  is well below 1.0, ranging between 0.25 and 0.5 for WSR-88D radars and 0.1 and 0.25 for CASA radars. While the consistency ratio of  $V_r$  is virtually unchanged between CNTL and NoMMP, the consistency ratio of  $Z$  is considerably higher in CNTL than in NoMMP at all radar sites throughout the assimilation period. Though the consistency ratio of  $Z$  for CNTL still remains below the optimal value of 1.0 at most radar sites, particularly late in the assimilation period, the higher consistency ratio values for  $Z$  in CNTL suggest that CNTL exhibits significantly less under-dispersion than NoMMP (Fig. 15).

Though ensemble spread in  $Z$  is increased significantly when a mixed-microphysics ensemble is used, ensemble spread of  $V_r$  is less impacted; this is believed to be due to the less direct link between the wind fields and microphysical states. These results are consistent with the findings of Meng and Zhang (2008), who noted greater impact to thermodynamic and moisture fields than to wind fields when assimilating rawinsonde data using an EnKF method, and also consistent with the findings of Fujita et al. (2007). Within a model, the microphysical scheme directly impacts microphysics species, which in turn directly affects the model estimate of reflectivity. By contrast, the microphysical scheme only influences the model wind field through indirect interactions. As a result, the use of a mixed-microphysics ensemble produces a

notable increase in ensemble spread of  $Z$ , but smaller increase in ensemble spread of  $V_r$ .

#### 4. Summary and discussion

In this paper, radar reflectivity and radial velocity from 4 experimental CASA X-band radars, in addition to data from existing operational WSR-88D radars, are assimilated to evaluate the impact of dense, low-level, high-resolution radar data on ensemble Kalman filter analysis of a convective system. The ARPS ensemble Kalman filter assimilation system, modified to enable a mixed-microphysics ensemble, is used to conduct a set of three experiments for the case of the non-supercellular, tornadic MCS that occurred over northern Texas and southwestern and central Oklahoma on 8-9 May 2007; this case was the first tornadic event observed by the then newly-deployed CASA network. During the event, one EF-0 and two EF-1 tornadoes were produced in association with a line-end vortex (LEV) embedded within the MCS. The effect of using a single microphysical scheme versus a mixture of microphysics schemes within the forecast ensemble as a means to increase ensemble spread and better capture the true atmospheric state within the analysis envelope is investigated. By assimilating radar data for one hour at 5 minute intervals, analyses were obtained of the reflectivity fields that were in general agreement with the observations in all three experiments presented. Physically realistic analyses of the flow fields were also obtained.

Inclusion of CASA data resulted in a noticeable improvement of the mean ensemble analysis, as evidenced by the improved representation of observed near-surface circulations within the CASA domain as compared to low-level observations from KCYR (Figs. 7, 8). In the control experiment (CNTL) which included additional CASA data and used a multi-microphysics ensemble, a time-height cross-section of vertical vorticity indicated a local near-

surface vorticity maximum occurring at the time of an observed, tornado-warned low-level circulation; this maximum was much weaker in the experiment in which no CASA data was assimilated (NoCASA). Comparison of observed and simulated radial velocity ( $V_r$ ) for the KCYR radar site shows a strong circulation at the two degree elevation angle in observations (Fig. 7a) and in CNTL (Fig. 7b), but only a weak circulation in NoCASA (Fig. 7c). Analysis of surface winds and cold pool intensity reveals a stronger surface circulation in CNTL (Fig. 8a), with enhanced inflow as compared to NoCASA (Fig. 8b) as well as a gust front structure more consistent with near-surface KCYR  $V_r$  observations (Fig. 8c). The most significant differences between CNTL and NoCASA are seen in the lowest few kilometers of the atmosphere; this is the region where WSR-88D coverage is poor and where CASA contributes most.

Assimilation of CASA data made a modest positive impact on average RMS innovation and ensemble spread statistics; assimilating CASA data resulted in a slight reduction in RMS innovation statistics at WSR-88D radar sites whose coverage areas overlapped the CASA IP1 domain (KTLX and KVN). This reduction was present in RMS innovation statistics for both radial velocity ( $V_r$ ) and radar reflectivity ( $Z$ ), though the reduction was larger for  $Z$ , and was greatest in the first six assimilation cycles. From the notable improvement in early cycles, we can conclude that assimilation of CASA data allowed the EnKF system to more quickly achieve a good estimate of the atmospheric state. With regard to ensemble spread of  $V_r$  and  $Z$ , however, assimilation of CASA data had very little impact.

The use of a mixed-microphysics ensemble resulted in increased spread within the ensemble, particularly for  $Z$ ; this effect was beneficial in reducing under-dispersion among ensemble members and in improving the statistical consistency of the EnKF analysis. In experiment CNTL, where a mixed-microphysics ensemble was used, the ensemble spread of  $Z$  at

all radar sites is greatly increased compared to experiment NoMMP, which used a single-microphysics scheme for all ensemble members. During much of the assimilation period, the ensemble spread of  $Z$  in CNTL was more than twice that of NoMMP. Compared to NoMMP, CNTL displayed slightly lower RMS innovation values for both  $V_r$  and  $Z$ , as well as a marked increase in the consistency ratio, demonstrating the ability of the mixed-microphysics ensemble in helping to alleviate under-dispersion of the analysis ensemble in CNTL. While still below the optimal value of approximately 1.0, the consistency ratio for  $Z$  in CNTL is much higher than that of NoMMP. Even in CNTL, however, under-dispersion is still present in  $Z$ , and all three experiments show marked under-dispersion in  $V_r$ , despite the application of rather large multiplicative covariance inflation of 25%. The use of a mixed-microphysics ensemble, while beneficial in alleviating under-dispersion in the ensemble, is not alone sufficient to counteract the low ensemble spread often observed in EnKF studies, at least for this case. Under-dispersion is a common problem in storm-scale data assimilation that deserves further investigation. Possible methods to address this issue include additive perturbations (Dowell and Wicker 2009) and adaptive inflation (Anderson 2007) techniques. To address under-dispersion in  $V_r$ , planetary boundary layer and subgrid-scale turbulence mixing parameterization perturbations might be beneficial; this can be a topic for future research.

For a tornadic system, such as the one in this study, a horizontal grid spacing of 2 km is clearly insufficient to fully resolve all important sub-storm-scale processes. While this resolution is able to capture the bookend vortex and low-level mesocyclone circulations observed in this case, a significantly smaller grid spacing (on the order of 100 m) would be necessary to capture tornado-scale circulations. Insufficient resolution may be another important cause of under-dispersion, because a significant part of the energy spectrum that can contribute significantly to

the ensemble dispersion may be missing (e.g., Nutter et al. 2004). In the future, we intend to investigate this issue by using much higher spatial resolutions; such an increase in resolution will require the use of an efficient parallel EnKF system. Another possible cause of under-dispersion is insufficient perturbation to the mesoscale environment in which the MCS is embedded. While we believe our domain is large enough for the lateral boundary condition to have only a minimal impact during the limited length of assimilation, storm-scale EnKF cycles nested within a mesoscale ensemble system have been shown, in general, to perform better (Lei et al. 2009). Since the primary goal of this study is to examine the impact of CASA radar data from the first tornadic case observed by the CASA IP-1 network using a data assimilation method that is still in the early stages of successful application to real storm cases, we believe the results presented in this paper meet our primary goal even though there remain a number of issues that merit further investigation.

Finally, we note the challenges of working with X-band Doppler radar data, perhaps the greatest of which is reflectivity attenuation. While S-band radars, such as the WSR-88D network suffer very little attenuation, even through heavy precipitation, attenuation at X-band is much more significant. An X-band beam from a CASA radar passing through heavy precipitation (50 dBZ or greater) for more than approximately 10 km is attenuated completely, leaving a “shadow” of near-zero reflectivity returns beyond the range where complete attenuation occurs. Additionally, even when attenuation is only partial, error within the attenuation correction algorithm leads to discrepancies between X-band and S-band observations of the same volume of the atmosphere (note that attenuation correction has been applied to CASA reflectivity data used in this study). To avoid assimilating spurious reflectivity in regions of complete attenuation, we used CASA data above a 20 dBZ threshold only; however,

doing so also eliminated the ability of the CASA radar data to suppress spurious convection, which has been shown to be one of the most valuable aspects of reflectivity data (Tong and Xue 2005). Finding effective ways to better correct for attenuation and to objectively identify and remove data associated with complete attenuation will likely improve the positive impact of CASA type data. A promising method proposed by Xue et al. (2009) will be tested with this case in the future.

*Acknowledgements:* This work was primarily supported by NSF grant EEC-0313747 as part of ERC CASA program. The second author was also supported by NSF grants AGS-0802888 and AGS-0738370, AGS-0608168, AGS-0750790, AGS-0941491, and OCI-0905040. The first author would like to personally acknowledge Daniel Dawson and Keith Brewster for assistance in troubleshooting the ARPS system, Jerry Brotzge for technical assistance in obtaining and formatting CASA radar data, and Robin Tanamachi for many helpful discussions regarding EnKF techniques. Most of the computations were performed at the OU Supercomputing Center for Education & Research (OSCER) at the University of Oklahoma (OU).

## References

- Aksoy, A., D. C. Dowell, and C. Snyder, 2009: A multi-case comparative assessment of the ensemble Kalman filter for assimilation of radar observations. Part I: Storm-scale analysis. *Monthly Weather Review*, **137**, 1805-1824.
- Aksoy, A., D. C. Dowell, and C. Snyder, 2010: A multi-case comparative assessment of the ensemble Kalman filter for assimilation of radar observations. Part I: Short-range ensemble forecasts. *Monthly Weather Review*, In press.
- Anderson, J. L., 2007: An adaptive covariance inflation error correction algorithm for ensemble filters. *Tellus A*, **59**, 210-224.
- Anderson, J. L. and S. L. Anderson, 1999: A Monte Carlo implementation of the nonlinear filtering problem to produce ensemble assimilations and forecasts. *Mon. Wea. Rev.*, **127**, 2741-2758.
- Bharadwaj, N., V. Chandrasekar, and F. Junyent, 2010: Signal Processing System for the CASA Integrated Project I Radars. *Journal of Atmospheric and Oceanic Technology*, **27**, 1440 - 1460.
- Brewster, K., 1996: Application of a Bratseth analysis scheme including Doppler radar data. *Preprints, 15th Conf. Wea. Anal. Forecasting*, Norfolk, VA, Amer. Meteor. Soc., 92-95.
- Brewster, K., M. Hu, M. Xue, and J. Gao, 2005: Efficient assimilation of radar data at high resolution for short-range numerical weather prediction. *WWRP Int. Symp. Nowcasting Very Short Range Forecasting*, CDROM 3.06.
- Brewster, K. A., K. W. Thomas, J. Brotzge, Y. Wang, D. Weber, and M. Xue, 2007: High resolution data assimilation of CASA X-band radar data for thunderstorm forecasting.

22nd Conf. Wea. Anal. Forecasting/18th Conf. Num. Wea. Pred., Salt Lake City, Utah,  
Amer. Meteor. Soc., CDROM 1B.1.

Brotzge, J., D. Westbrook, K. Brewster, K. Hondl, and M. Zink, 2005: The Meteorological  
Command and Control Structure of a Dynamic, Collaborative, Automated Radar Network.  
*21st International Conf. on Interactive Information Processing Systems (IIPS) for Meteor.,  
Ocean., and Hydrology*, American Meteorological Society.

Brotzge, J., K. Hundle, B. Philips, L. Lemon, E. Bass, D. Rude, and D. Andra, Jr., 2010a:  
Evaluation of Distributed Collaborative Adaptive Sensing for detection of low-level  
circulations and implications for severe weather operations. *Wea. Forecasting*, **25**, 173-  
189.

Brotzge, J., L.R. Lemon, 2010b: An anticyclonic tornado observed 10 May 2010 with CASA  
radar. *25th Conf. Severe Local Storms*, Amer. Meteor. Soc., Paper P10.11.

Chandrasekar, V., S. Lim, N. Bharadwaj, W. Li, D. McLaughlin, V. N. Bringi, and E. Gorgucci,  
2004: Principles of networked weather radar operation at attenuating frequencies. *Proc.  
Third European Conf. on Radar Meteorology and Hydrology*, 109-114.

Crum, T. D., R. L. Albert, and D. W. Burgess, 1993: Recording, archiving, and using WSR-88D  
data. *Bull. Amer. Meteor. Soc.*, **74**, 645-653.

Dowell, D., G. Romine, and C. Snyder, 2010: Ensemble Storm Scale Data Assimilation and  
Prediction for Severe Convective Storms. *25th Conference on Severe Local Storms*, Amer.  
Meteor. Soc., Paper 9.5.

Dowell, D., F. Zhang, L. J. Wicker, C. Snyder, and N. A. Crook, 2004a: Wind and temperature  
retrievals in the 17 May 1981 Arcadia, Oklahoma supercell: Ensemble Kalman filter  
experiments. *Mon. Wea. Rev.*, **132**, 1982-2005.

- Dowell, D. C. and H. B. Bluestein, 1997: The Arcadia, Oklahoma, storm of 17 May 1981: Analysis of a supercell during Tornadogenesis. *Mon. Wea. Rev.*, **125**, 2562-2582.
- Dowell, D. C. and L. J. Wicker, 2009: Additive noise for storm-scale ensemble data assimilation. *Journal of Atmospheric and Oceanic Technology*, 911-927. DOI: 10.1175/2008JTECHA1156.1.
- Dowell, D. C., L. J. Wicker, and D. J. Stensrud, 2004b: High-resolution analyses of the 8 May 2003 Oklahoma City storm. Part II: EnKF data assimilation and forecast experiments. *Preprints, 22nd Conf. on Severe Local Storms*, Hyannis, MA,, Amer. Meteor. Soc., CDROM, 12.5.
- Evensen, G., 1994: Sequential data assimilation with a nonlinear quasi-geostrophic model using Monte Carlo methods to forecast error statistics. *J. Geophys. Res.*, **99**, 10143-10162.
- Evensen, G., 2003: The ensemble Kalman filter: Theoretical formulation and practical implementation. *Ocean Dynamics*, **53**, 343-367.
- Fujita, T., D. J. Stensrud, and D. C. Dowell, 2007: Surface data assimilation using an ensemble Kalman filter approach with initial condition and model physics uncertainties. *Mon. Wea. Rev.*, **135**, 1846-1868.
- Fujita, T. T., 1978: Manual of downburst identification for project Nimrod. 104.
- Ge, G., J. Gao, K. Brewster, and M. Xue, 2010: Impacts of beam broadening and earth curvature on 3D variational radar data assimilation of radial velocity with two Doppler radars. *J. Atmos. Ocean Tech.*, **27**, 617-636.
- Hong, S.-Y. and J.-O. J. Lim, 2006: The WRF single-moment 6-class microphysics scheme (WSM6). *J. Korean Meteor. Soc.*, **42**, 129-151.
- Houze, R. A., Jr., S. A. Rutledge, M. I. Biggerstaff, and B. F. Smull, 1989: Interpretation of

Doppler weather radar displays of midlatitude mesoscale convective systems. *Bull. Amer. Meteor. Soc.*, **70**, 607-619.

Hu, M., M. Xue, J. Gao, and K. Brewster, 2006: 3DVAR and cloud analysis with WSR-88D level-II data for the prediction of Fort Worth tornadic thunderstorms. Part II: Impact of radial velocity analysis via 3DVAR. *Mon. Wea. Rev.*, **134**, 699-721.

Jung, Y., G. Zhang, and M. Xue, 2008: Assimilation of simulated polarimetric radar data for a convective storm using ensemble Kalman filter. Part I: Observation operators for reflectivity and polarimetric variables. *Mon. Wea. Rev.*, **136**, 2228-2245.

Klemp, J. B. and R. Rotunno, 1983: A study of the tornadic region within a supercell thunderstorm. *J. Atmos. Sci.*, **40**, 359-377.

Klemp, J. B., R. B. Wilhelmson, and P. S. Ray, 1981: Observed and numerically simulated structure of a mature supercell thunderstorm. *J. Atmos. Sci.*, **38**, 1558-1580.

Kumjian, M. R. and A. V. Ryzhkov, 2008: Polarimetric signatures in supercell thunderstorms. *J. Appl. Meteor. Climatol.*, **47**, 1940-1961.

Lei, T., M. Xue, and T. Yu, 2009: Multi-scale analysis and prediction of the 8 May 2003 Oklahoma City tornadic supercell storm assimilating radar and surface network data using EnKF. *Extended abstract, 13th Conf. of IOAS-AOLS, AMS Meetings 2008*, Paper 6.4.

Lin, Y.-L., R. D. Farley, and H. D. Orville, 1983: Bulk parameterization of the snow field in a cloud model. *J. Climat. Appl. Meteor.*, **22**, 1065-1092.

Lorenz, E. N., 1969: The predictability of a flow which possesses many scales of motion. *Tellus*, **21**, 289-307.

Markowski, P. M., J. M. Straka, and E. N. Rasmussen, 2002: Direct surface thermodynamic observations within the rear-flank downdrafts of nontornadic and tornadic supercells.

*Mon. Wea. Rev.*, **130**, 1692-1721.

- McLaughlin, D., D. Pepyne, V. Chandrasekar, B. Philips, J. Kurose, M. Zink, K. Droege, S. Cruz-Pol, F. Junyent, J. Brotzge, D. Westbrook, N. Bharadwaj, Y. Wang, E. Lyons, K. Hondl, Y. Liu, E. Knapp, M. Xue, A. Hopf, K. Kloesel, A. DeFonzo, P. Kollias, K. Brewster, R. Contreras, B. Dolan, T. Djaferis, E. Insanic, S. Frasier, and F. Carr, 2009: Short-wavelength technology and the potential for distributed networks of small radar systems. *Bull. Amer. Meteor. Soc.*, **90**, 1797-1817.
- Meng, Z. and F. Zhang, 2007: Tests of an Ensemble Kalman Filter for Mesoscale and Regional-Scale Data Assimilation. Part II: Imperfect Model Experiments *Mon. Wea. Rev.*, **135**, 1403–1423
- Nutter, P., D. Stensrud, and M. Xue, 2004: Effects of coarsely-resolved and temporally-interpolated lateral boundary conditions on the dispersion of limited-area ensemble forecasts. *Mon. Wea. Rev.*, **132**, 2358-2377.
- Rotunno, R., 1993: Supercell thunderstorm modeling and theory. The Tornado: Its Structure, Dynamics, Hazards, and Prediction, Geophys. Monogr., No. 79. *Amer. Geophys. Union*, **57-73**.
- Rotunno, R., J. B. Klemp, and M. L. Weisman, 1988: A theory for strong long-lived squall lines. *J. Atmos. Sci.*, **45**, 463-485.
- Schenkman, A., M. Xue, A. Shapiro, K. Brewster, and J. Gao, 2010: The analysis and prediction of the 8-9 May 2007 Oklahoma tornadic mesoscale convective system by assimilating WSR-88D and CASA radar data using 3DVAR. *Mon. Wea. Rev.*, **139**, 224-246.
- Schultz, P., 1995: An explicit cloud physics parameterization for operational numerical weather prediction. *Mon. Wea. Rev.*, **123**, 3331-3343.

- Snook, N. and M. Xue, 2008: Effects of microphysical drop size distribution on tornadogenesis in supercell thunderstorms. *Geophys. Res. Letters*, **35**, L24803, doi:10.1029/2008GL035866.
- Snyder, C. and F. Zhang, 2003: Assimilation of simulated Doppler radar observations with an ensemble Kalman filter. *Mon. Wea. Rev.*, **131**, 1663-1677.
- Sun, J. and N. A. Crook, 1997: Dynamical and microphysical retrieval from Doppler radar observations using a cloud model and its adjoint. Part I: Model development and simulated data experiments. *J. Atmos. Sci.*, **54**, 1642-1661.
- Sun, J. and N. A. Crook, 1998: Dynamical and Microphysical Retrieval from Doppler Radar Observations Using a Cloud Model and Its Adjoint. Part II: Retrieval Experiments of an Observed Florida Convective Storm. *J. Atmos. Sci.*, **55**, 835-852.
- Sun, J., D. W. Flicker, and D. K. Lilly, 1991: Recovery of three-dimensional wind and temperature fields from simulated single-Doppler radar data. *J. Atmos. Sci.*, **48**, 876-890.
- Tao, W.-K. and J. Simpson, 1993: Goddard cumulus ensemble model. Part I: Model description. *Terres. Atmos. Ocean Sci.*, **4**, 35-72.
- Tong, M., 2006: Ensemble Kalman filer assimilation of Doppler radar data for the initialization and prediction of convective storms, School of Meteorology, University of Oklahoma, 243.
- Tong, M. and M. Xue, 2005a: Simultaneous retrieval of microphysical parameters and atmospheric state variables with radar data and ensemble Kalman filter method. *Preprint, 17th Conf. Num. Wea. Pred.*, Washington DC, Amer. Meteor. Soc., CDROM P1.30.
- Tong, M. and M. Xue, 2005b: Ensemble Kalman filter assimilation of Doppler radar data with a compressible nonhydrostatic model: OSS Experiments. *Mon. Wea. Rev.*, **133**, 1789-1807.

- Tong, M. and M. Xue, 2008a: Simultaneous estimation of microphysical parameters and atmospheric state with radar data and ensemble square-root Kalman filter. Part II: Parameter estimation experiments. *Mon. Wea. Rev.*, **136**, 1649–1668.
- Tong, M. and M. Xue, 2008b: Simultaneous estimation of microphysical parameters and atmospheric state with radar data and ensemble square-root Kalman filter. Part I: Sensitivity analysis and parameter identifiability. *Mon. Wea. Rev.*, **136**, 1630–1648.
- Trapp, R. J., S. A. Tessendorf, E. S. Godfrey, and H. E. Brooks, 2005: Tornadoes from Squall Lines and Bow Echoes. Part I: Climatological Distribution. *Wea. Forecasting*, **20**, 23-34.
- Weisman, M. L., 1993: The genesis of severe long-lived bow-echoes. *J. Atmos. Sci.*, **50**, 645-670.
- Whitaker, J. S. and T. M. Hamill, 2002: Ensemble data assimilation without perturbed observations. *Mon. Wea. Rev.*, **130**, 1913-1924.
- Wood, V. T. and R. A. Brown, 1997: Effects of radar sampling on single-Doppler velocity signatures of mesocyclones and tornadoes. *Wea. Forecast.*, **12**, 928-938.
- Xue, M., K. K. Droegemeier, and V. Wong, 2000: The Advanced Regional Prediction System (ARPS) - A multiscale nonhydrostatic atmospheric simulation and prediction tool. Part I: Model dynamics and verification. *Meteor. Atmos. Physics*, **75**, 161-193.
- Xue, M., M. Tong, and K. K. Droegemeier, 2006: An OSSE framework based on the ensemble square-root Kalman filter for evaluating impact of data from radar networks on thunderstorm analysis and forecast. *J. Atmos. Ocean Tech.*, **23**, 46–66.
- Xue, M., M. Tong, and G. Zhang, 2009: Simultaneous state estimation and attenuation correction for thunderstorms with radar data using an ensemble Kalman filter: Tests with simulated data. *Q. J. Roy. Meteor. Soc.*, **135**, 1409-1423.
- Xue, M., D.-H. Wang, J.-D. Gao, K. Brewster, and K. K. Droegemeier, 2003: The Advanced

Regional Prediction System (ARPS), storm-scale numerical weather prediction and data assimilation. *Meteor. Atmos. Physics*, **82**, 139-170.

Xue, M., K. K. Droege, V. Wong, A. Shapiro, K. Brewster, F. Carr, D. Weber, Y. Liu, and D.-H. Wang, 2001: The Advanced Regional Prediction System (ARPS) - A multiscale nonhydrostatic atmospheric simulation and prediction tool. Part II: Model physics and applications. *Meteor. Atmos. Phy.*, **76**, 143-165.

Xue, M., F. Kong, D. Weber, K. W. Thomas, Y. Wang, K. Brewster, K. K. Droege, J. S. K. S. J. Weiss, D. R. Bright, M. S. Wandishin, M. C. Coniglio, and J. Du, 2007: CAPS realtime storm-scale ensemble and high-resolution forecasts as part of the NOAA Hazardous Weather Testbed 2007 spring experiment. *22nd Conf. Wea. Anal. Forecasting/18th Conf. Num. Wea. Pred.*, Amer. Meteor. Soc., CDROM 3B.1.

Zhang, F., C. Snyder, and J. Sun, 2004: Impacts of initial estimate and observations on the convective-scale data assimilation with an ensemble Kalman filter. *Mon. Wea. Rev.*, **132**, 1238-1253.

## List of Figures

Fig. 1. Summary of tornadic activity associated with the 8-9 May 2007 convective system.

CASA radars (indicated by black squares) are identified; 40 km CASA range rings are indicated in gray. Oklahoma counties are shown and labeled. Confirmed tornadoes during the 9 May 2007 case are indicated by black triangles with the time of occurrence noted (all times shown are for 9 May 2007). The tornadoes reported at 0354 and 0443 UTC were of EF-1 intensity on the enhanced Fujita scale; the tornado reported at 0426 UTC was of EF-0 intensity.

Fig. 2. Composite radar reflectivity mosaic (dBZ) as observed by WSR-88D radars KAMA, KDYX, KFWS, KLBB, and KTLX at (a) 0000 UTC, (b) 0100 UTC, (c) 0200 UTC, (d) 0300 UTC, (e) 0400 UTC, and (f) 0500 UTC, 9 May 2007. 30 km CASA radar range rings are included for reference. Urban boundaries are shown in purple. The black box surrounding the CASA radar network in panel (a) denotes the CASA subdomain used for RMS innovation and spread calculations and updraft flux analyses. WSR-88D radar sites are indicated in panel (a).

Fig. 3. Flow diagram for experiments CNTL, NoMMP, and NoCASA. Initial forecasts were started at 0000 UTC on 9 May 2007. The shaded area indicates the period during which radar data were assimilated, from 0100 UTC to 0200 UTC.

Fig. 4. Composite radar reflectivity (dBZ) of the final ensemble mean analysis state at 0200 UTC 9 May 2007 for (a) CNTL, (b) NoMMP, and (c) NoCASA; also (d) composite radar reflectivity mosaic (dBZ) observed by WSR-88D radars KAMA, KDYX, KFWS, KLBB, and KTLX at

0200 UTC 9 May 2007. 30 km CASA radar range rings are included for reference.

Fig. 5. Plots of composite radar reflectivity (color-fill) and the horizontal wind field (vectors) at 1 km above ground level for the final ensemble mean analysis states of (a) CNTL, (b) NoMMP, and (c) NoCASA at 0200 UTC. 30 km CASA range rings and 60 km WSR-88D range rings are shown for reference.

Fig. 6. Time-height plot of maximum vertical vorticity ( $s^{-1}$ ) for the ensemble mean forecast (a) and analysis (b) of CNTL, and the forecast (c) and analysis (d) of NoCASA during the analysis period. Time is denoted in seconds since forecast initialization and ranges from 3900 s (0105 UTC) to 7200 s (0200 UTC). Height is shown in kilometers above ground level.

Fig. 7. Radial velocity for the 0140 UTC at the 2 degree elevation (a) as observed by CASA radar KCYR, and simulated from the 0140 UTC EnKF analyses of (b) CNTL and (c) NoCASA. The arrows highlight the circulation in the region of the tornado-warned mesovortex.

Fig. 8. Horizontal winds (barbs) and potential temperature (shaded) at the first model level above the surface near CASA radar KCYR for the 0140 UTC ensemble mean analysis in (a) CNTL and (b) NoCASA . The position of a gust front associated with the embedded mesovortex is indicated. Also shown are (c) full-resolution radial velocity observations from the 2° elevation of CASA radar KCYR shortly before 0140 UTC. The gust front position indicated by the radial velocity observations is indicated by the yellow line.

Fig. 9. (a) Total updraft mass flux profiles within the CASA subdomain (as denoted in Fig. 2a) at 0140 UTC for experiments CNTL and NoCASA. Histograms of vertical velocity exceeding  $4 \text{ m s}^{-1}$  within updraft regions in the CASA subdomain are plotted for (b) CNTL and (c) NoCASA.

Fig. 10. Average root-mean-square (RMS) innovation (solid lines) and spread (dotted lines) of radial velocity (in  $\text{m s}^{-1}$ ) for WSR-88D radars KTLX and KVN, as well as all 4 CASA radars for experiments CNTL (black lines) and NoCASA (gray lines) calculated every 5 minutes during the assimilation period. Calculations were limited to the CASA verification domain indicated in Fig. 2a at locations where either observed or model reflectivity is greater than or equal to 15 dBZ. The assimilation period lasts from 0100 UTC (3600 seconds) to 0200 UTC (7200 seconds of model time).

Fig. 11. As Fig. 8, but for radar reflectivity (in dBZ) instead of for radial velocity.

Fig. 12. Consistency ratio of Z (solid lines) and Vr (short dashed lines) for two WSR-88D radars (KTLX and KVN) and 4 CASA radars for experiments CNTL (black lines) and NoCASA (gray lines) calculated every 5 minutes during the assimilation period. Calculations were limited to the CASA verification domain indicated in Fig. 2a. The assimilation period lasts from 0100 UTC (3600 seconds of model time) to 0200 UTC (7200 seconds of model time). The thin, horizontal gray dashed line indicates the theoretically ideal consistency ratio of 1.0.

Fig. 13. As Fig. 10, but for experiments CNTL (black lines) and NoMMP (gray lines) including WSR-88D radars KAMA, KDYX, and KLBB and performing calculations over the entire model

domain.

Fig. 14. As Fig. 11, but for radar reflectivity (in dBZ) instead of radial velocity.

Fig. 15. As Fig. 12, but for experiments CNTL (black lines) and NoMMP (gray lines) including WSR-88D radars KAMA, KDYX, and KLBB and performing calculations over the entire model domain.

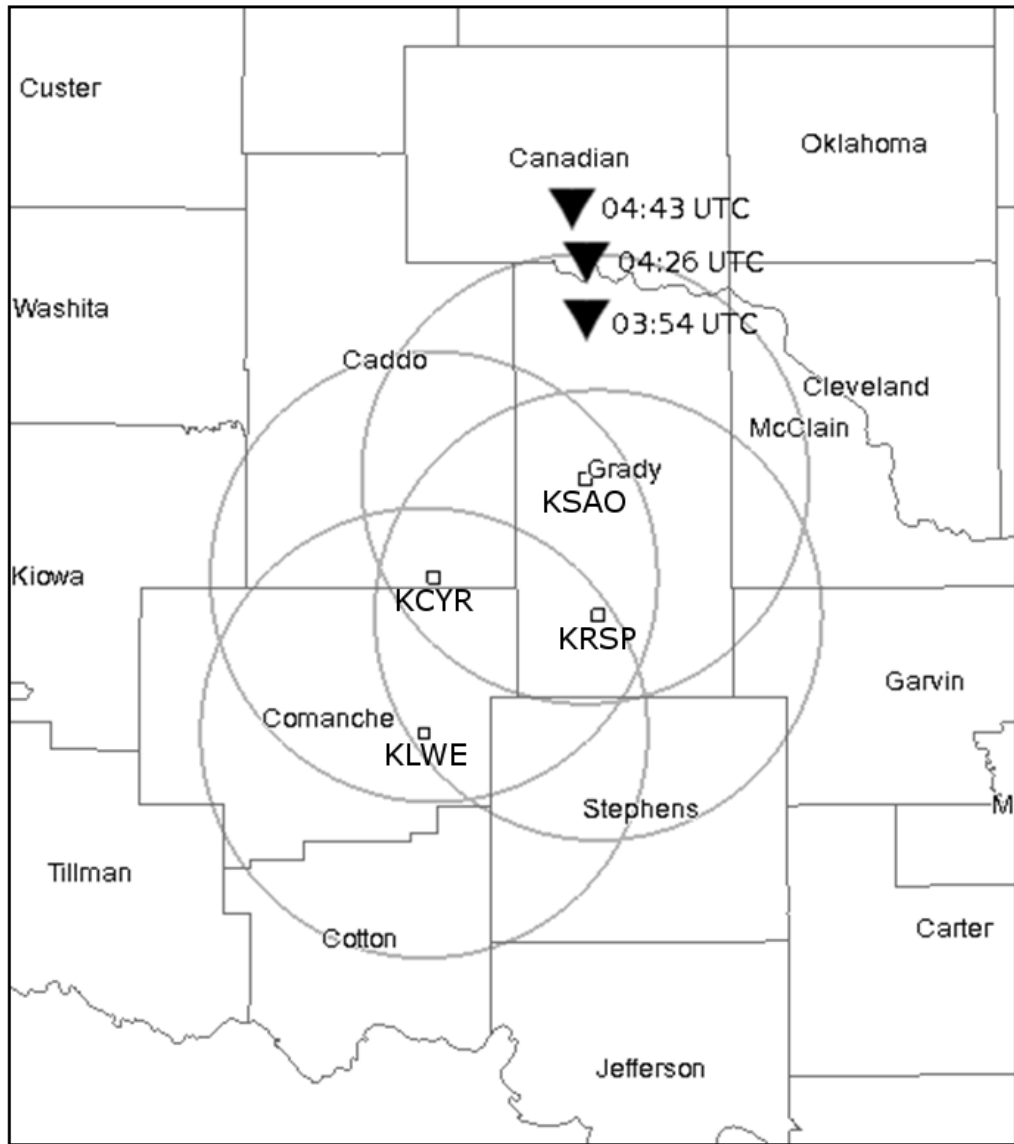


Fig. 1. Summary of tornadic activity associated with the 8-9 May 2007 convective system. CASA radars (indicated by black squares) are identified; 40 km CASA range rings are indicated in gray. Oklahoma counties are shown and labeled. Confirmed tornadoes during the 9 May 2007 case are indicated by black triangles with the time of occurrence noted (all times shown are for 9 May 2007). The tornadoes reported at 0354 and 0443 UTC were of EF-1 intensity on the enhanced Fujita scale; the tornado reported at 0426 UTC was of EF-0 intensity.

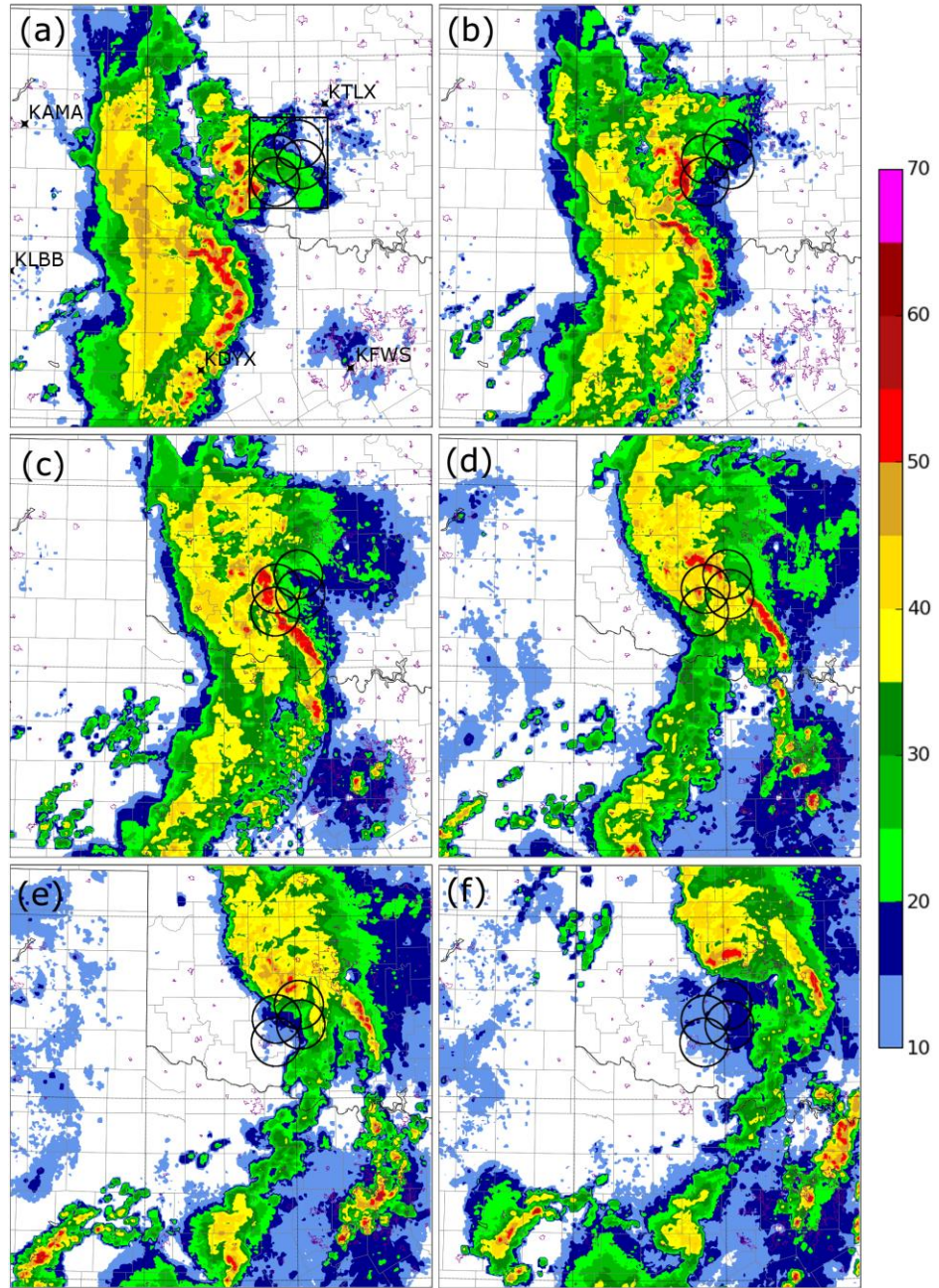


Fig. 2. Composite radar reflectivity mosaic (dBZ) as observed by WSR-88D radars KAMA, KDXY, KFWS, and KLBB at (a) 0000 UTC, (b) 0100 UTC, (c) 0200 UTC, (d) 0300 UTC, (e) 0400 UTC, and (f) 0500 UTC, 9 May 2007. 30 km CASA radar range rings are included for reference. Urban boundaries are shown in purple. The black box surrounding the CASA radar network in panel (a) denotes the CASA subdomain used for RMS innovation and spread calculations and updraft flux analyses. WSR-88D radar sites are indicated in panel (a).

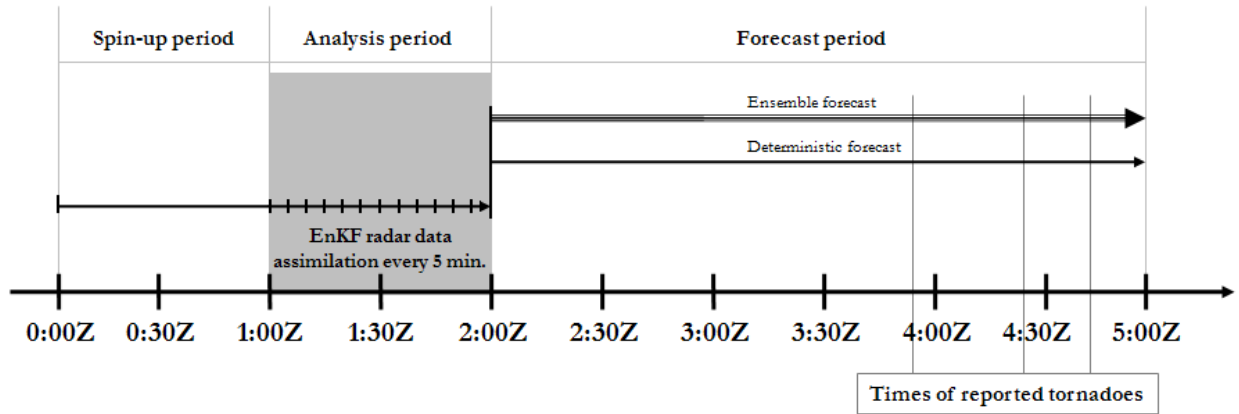


Fig. 3. Flow diagram for experiments CNTL, NoMMP, and NoCASA. Initial forecasts were started at 0000 UTC on 9 May 2007. The shaded area indicates the period during which radar data were assimilated, from 0100 UTC to 0200 UTC.

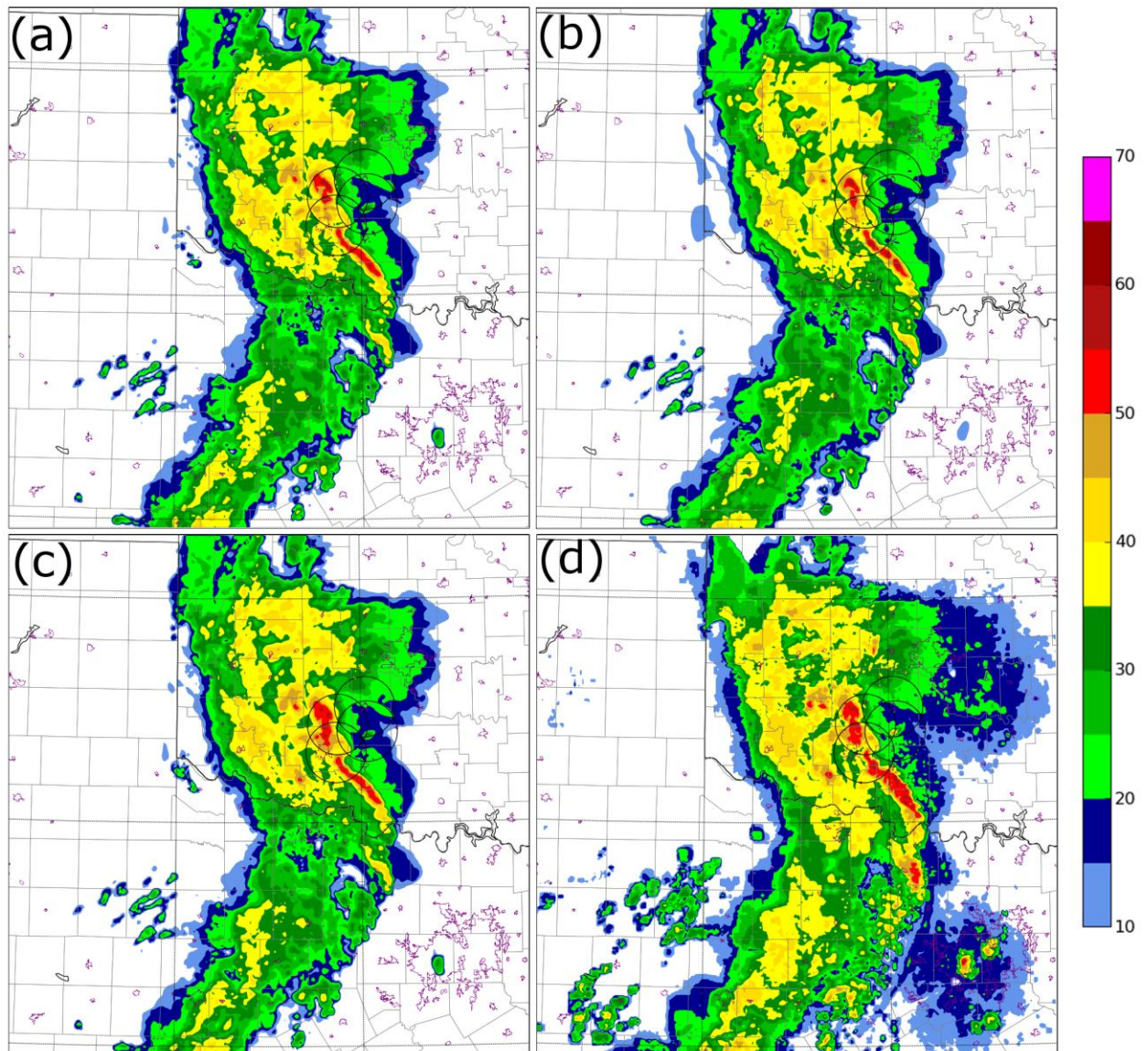


Fig. 4. Composite radar reflectivity (dBZ) of the final ensemble mean analysis state at 0200 UTC 9 May 2007 for (a) CNTL, (b) NoMMP, and (c) NoCASA; also (d) composite radar reflectivity mosaic (dBZ) observed by WSR-88D radars KAMA, KDYX, KFWS, KLBB, and KTLX at 0200 UTC 9 May 2007. 30 km CASA radar range rings are included for reference.

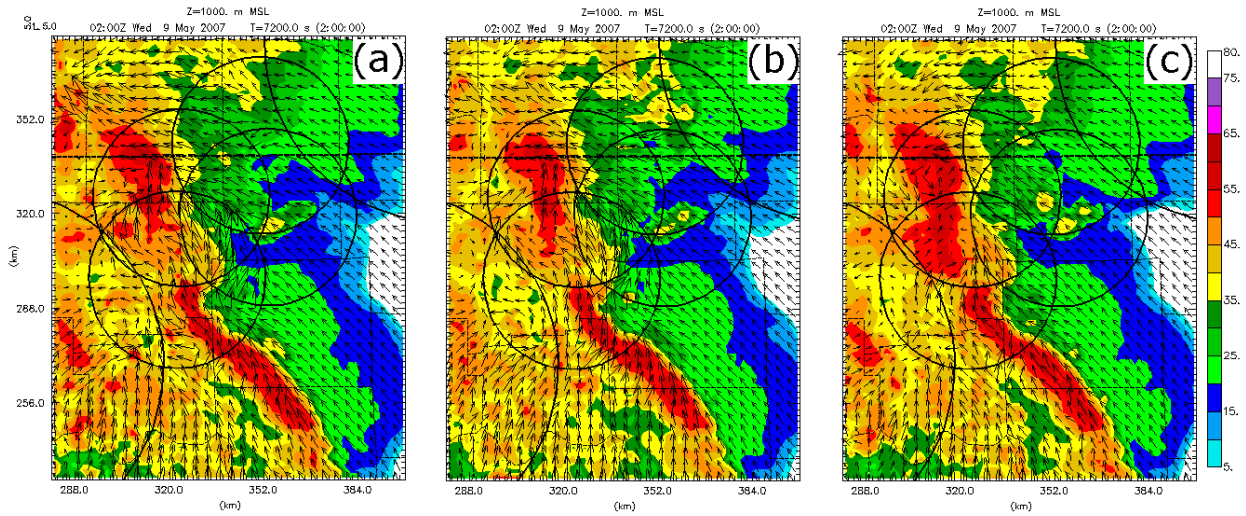


Fig. 5. Plots of composite radar reflectivity (color-fill) and the horizontal wind field (vectors) at 1 km above ground level for the final ensemble mean analysis states of (a) CNTL, (b) NoMMP, and (c) NoCASA at 0200 UTC. 30 km CASA range rings and 60 km WSR-88D range rings are shown for reference.

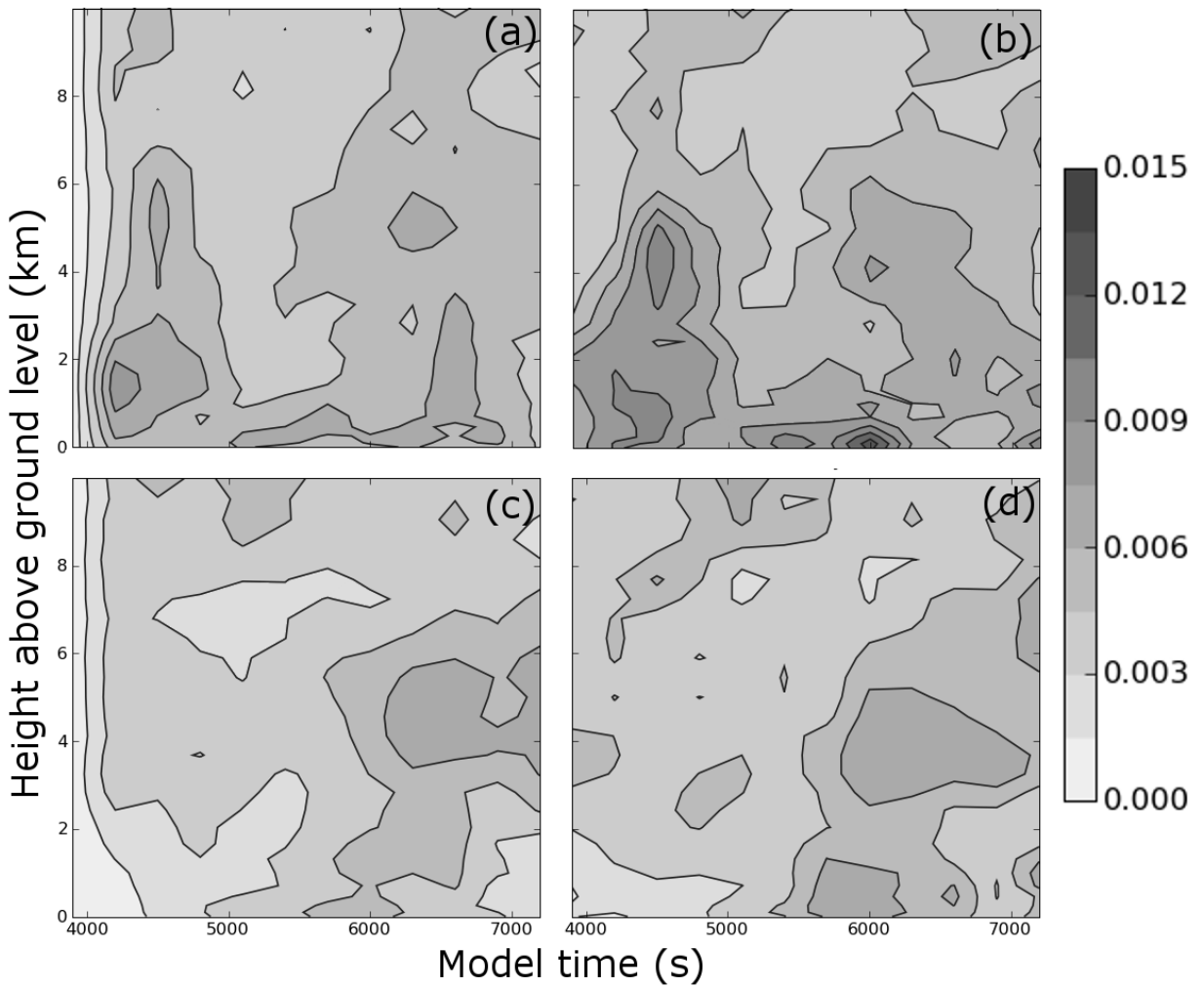


Fig. 6. Time-height plot of maximum vertical vorticity ( $\text{s}^{-1}$ ) for the ensemble mean forecast (a) and analysis (b) of CNTL, and the forecast (c) and analysis (d) of NoCASA during the analysis period. Time is denoted in seconds since forecast initialization and ranges from 3900 s (0105 UTC) to 7200 s (0200 UTC). Height is shown in kilometers above ground level.

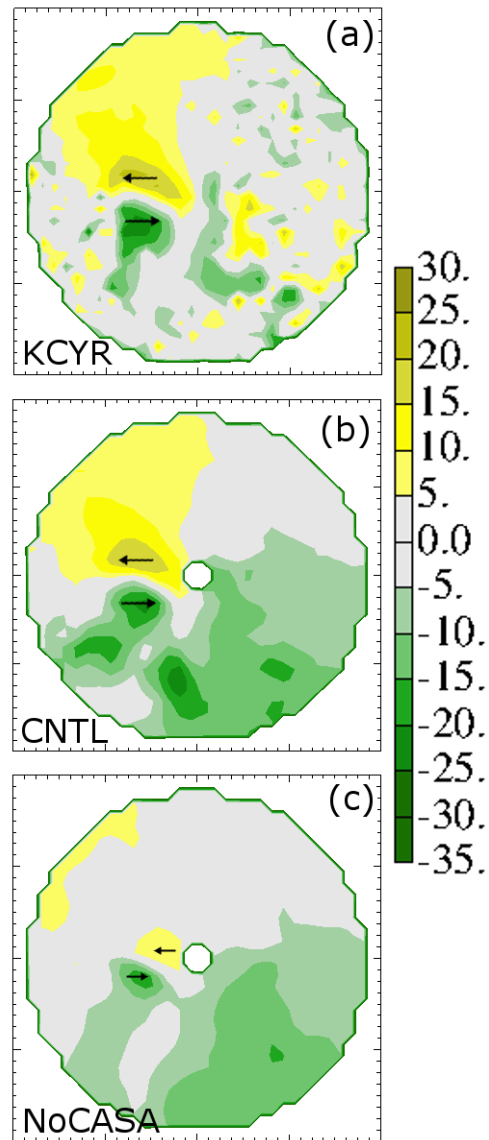


Fig. 7. Radial velocity for the 0140 UTC at the 2 degree elevation (a) as observed by CASA radar KCYR, and simulated from the 0140 UTC EnKF analyses of (b) CNTL and (c) NoCASA. The arrows highlight the circulation in the region of the tornado-warmed mesovortex.

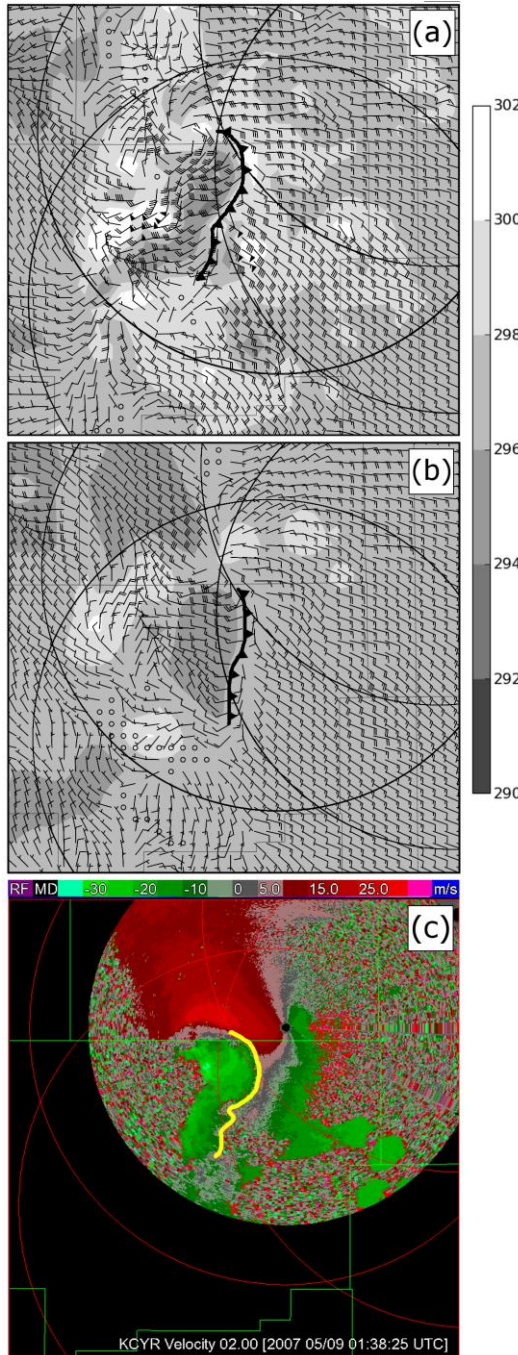


Fig. 8. Horizontal winds (barbs) and potential temperature (shaded) at the first model level above the surface near CASA radar KCYR for the 0140 UTC ensemble mean analysis in (a) CNTL and (b) NoCASA. The position of a gust front associated with the embedded mesovortex is indicated. Also shown are (c) full-resolution radial velocity observations from the  $2^{\circ}$  elevation of CASA radar KCYR shortly before 0140 UTC. The gust front position indicated by the radial velocity observations is indicated by the yellow line.

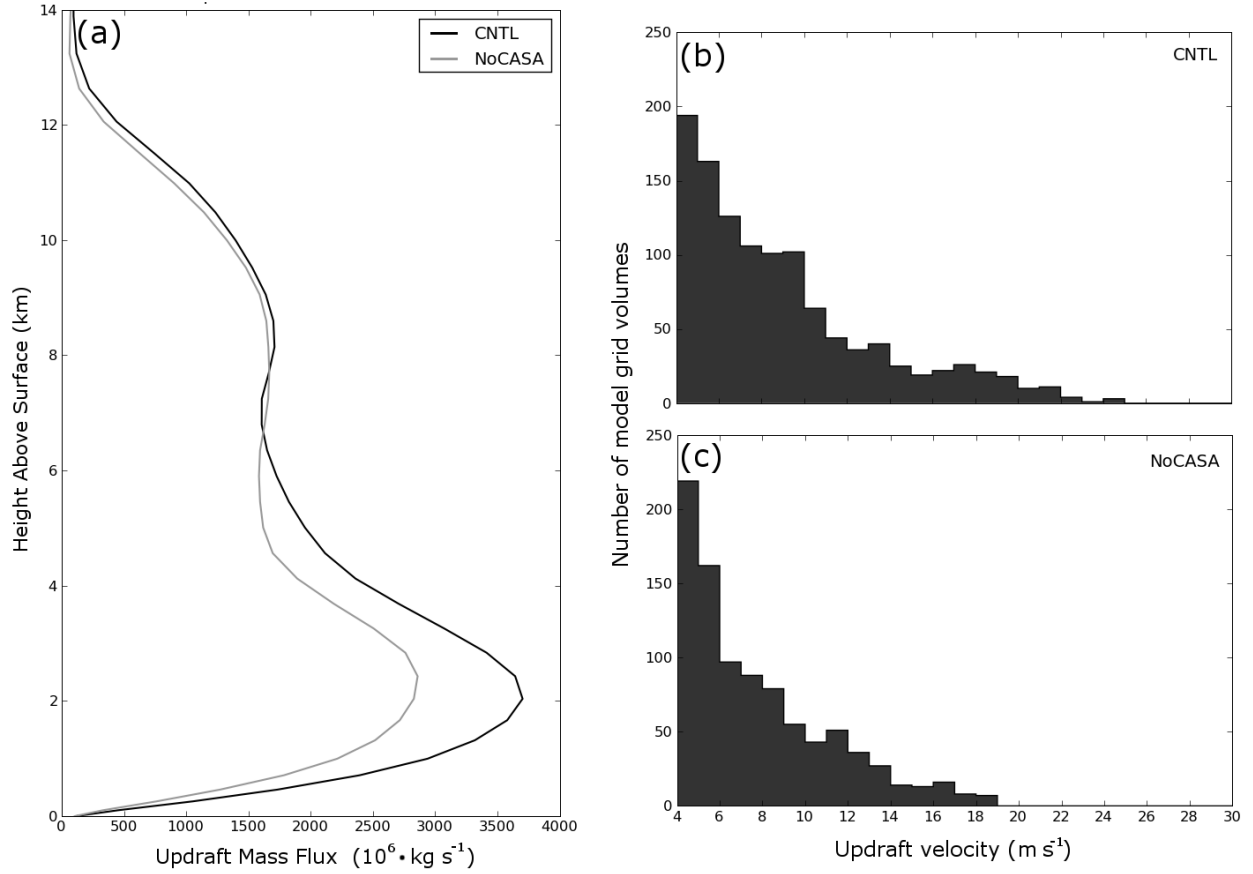


Fig. 9. (a) Total updraft mass flux profiles within the CASA subdomain (as denoted in Fig. 2a) at 0140 UTC for experiments CNTL and NoCASA. Histograms of vertical velocity exceeding  $4 \text{ m s}^{-1}$  within updraft regions in the CASA subdomain are plotted for (b) CNTL and (c) NoCASA.

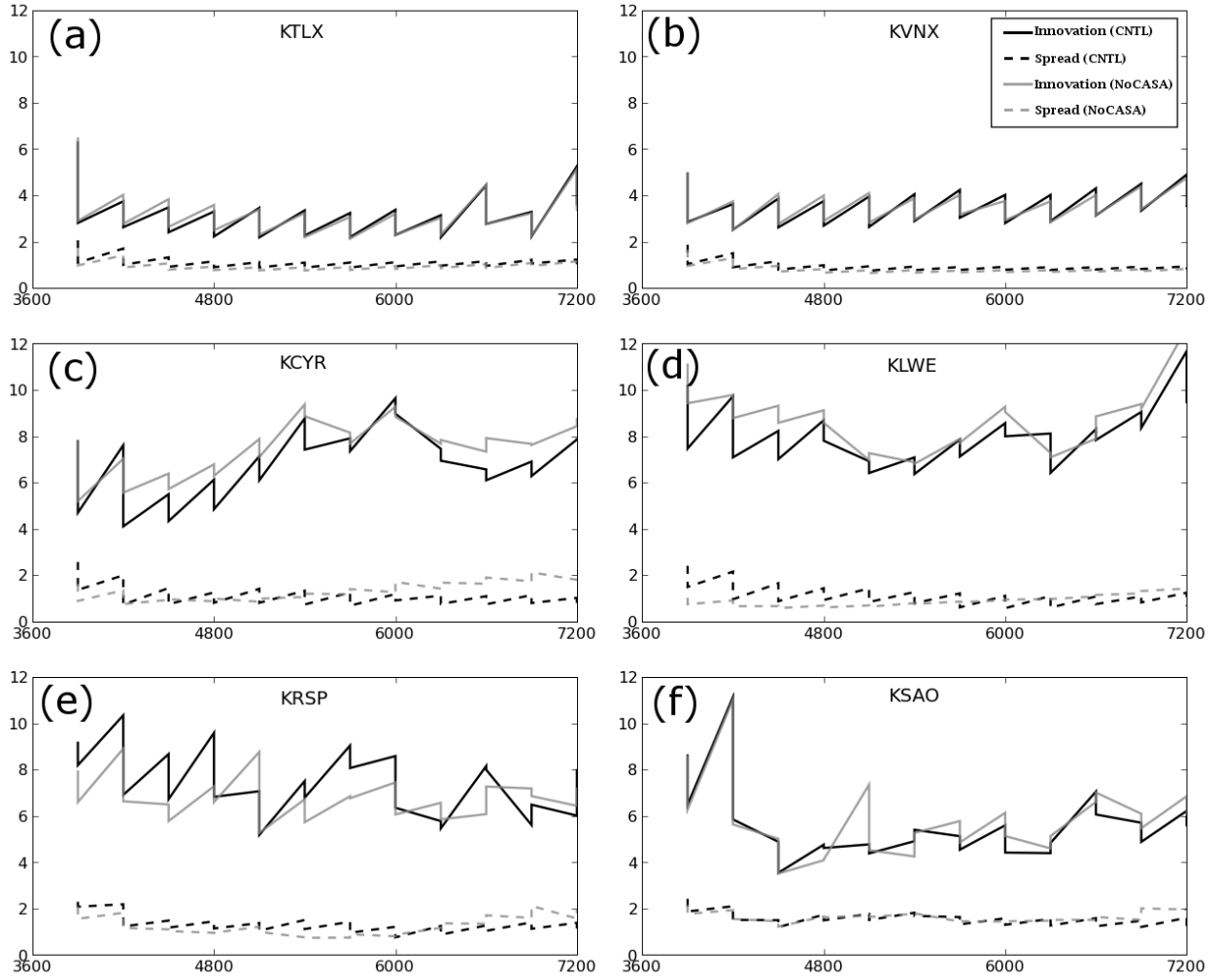


Fig. 10. Average root-mean-square (RMS) innovation (solid lines) and spread (dotted lines) of radial velocity (in  $\text{m s}^{-1}$ ) for WSR-88D radars KTLX and KVNX, as well as all 4 CASA radars for experiments CRTL (black lines) and NoCASA (gray lines) calculated every 5 minutes during the assimilation period. Calculations were limited to the CASA verification domain indicated in Fig. 2a at locations where either observed or model reflectivity is greater than or equal to 15 dBZ. The assimilation period lasts from 0100 UTC (3600 seconds) to 0200 UTC (7200 seconds of model time).

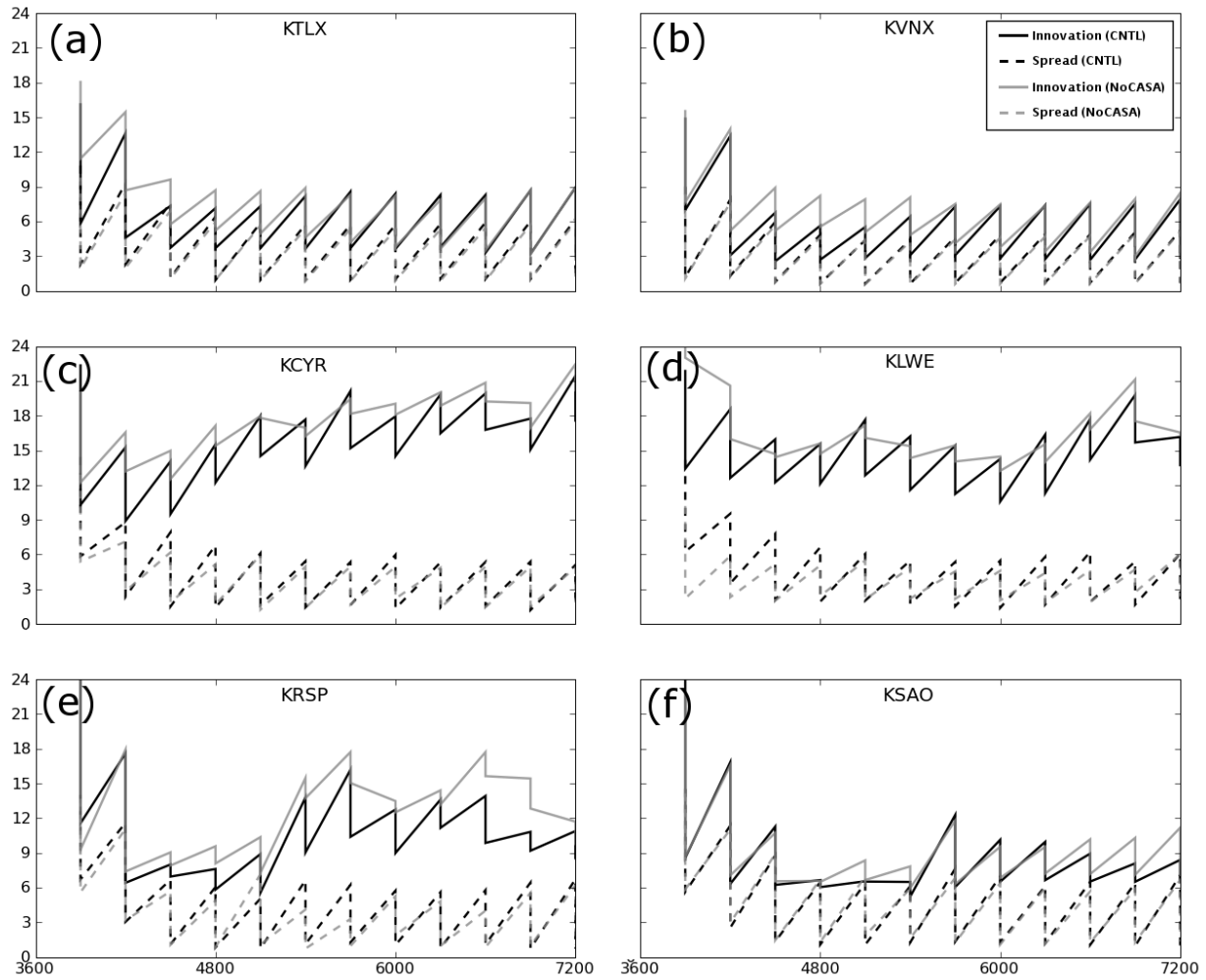


Fig. 11. As Fig. 8, but for radar reflectivity (in dBZ) instead of for radial velocity.

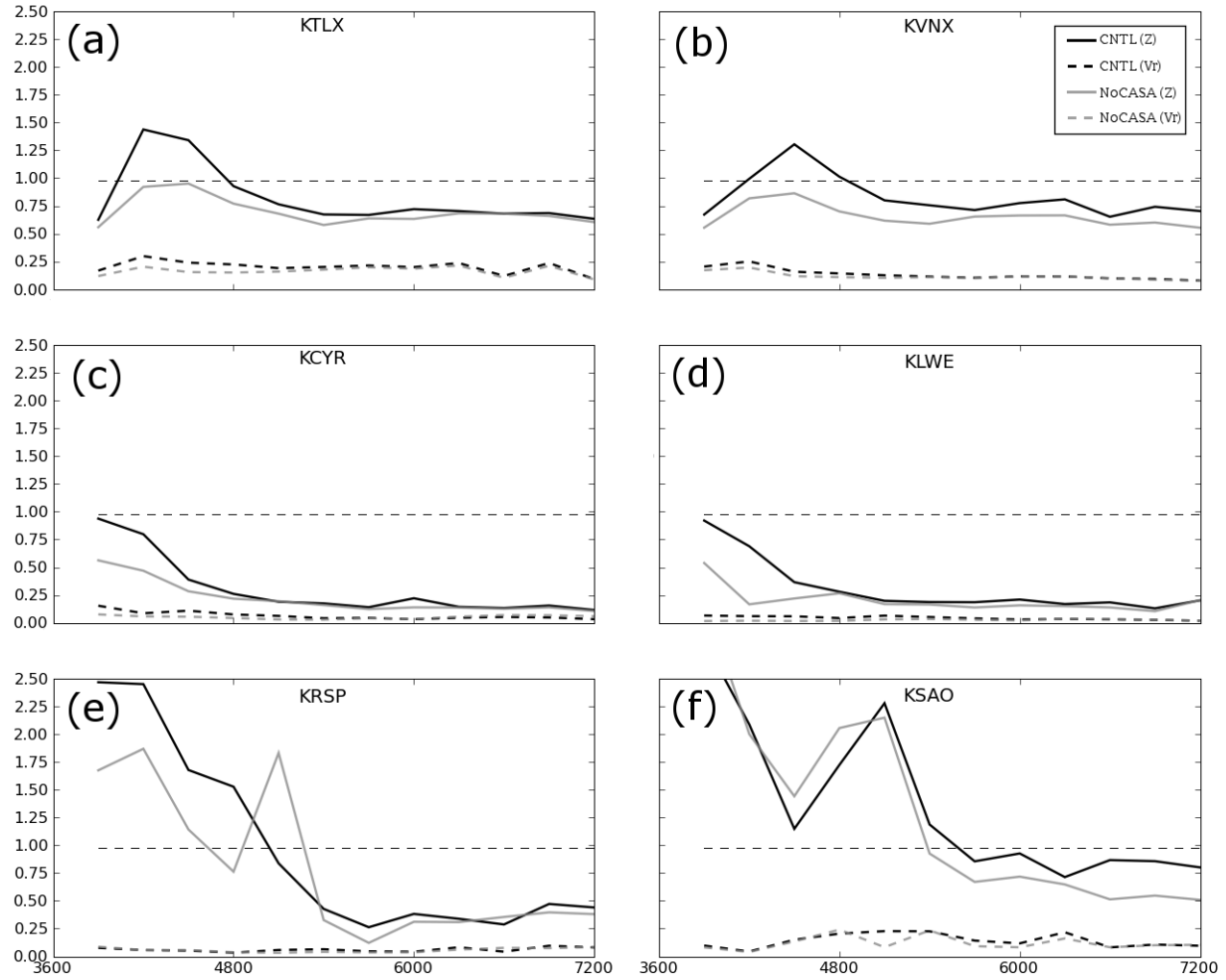


Fig. 12. Consistency ratio of Z (solid lines) and V<sub>r</sub> (short dashed lines) for two WSR-88D radars (KTLX and KVN) and 4 CASA radars for experiments CNTL (black lines) and NoCASA (gray lines) calculated every 5 minutes during the assimilation period. Calculations were limited to the CASA verification domain indicated in Fig. 2a. The assimilation period lasts from 0100 UTC (3600 seconds of model time) to 0200 UTC (7200 seconds of model time). The thin, horizontal gray dashed line indicates the theoretically ideal consistency ratio of 1.0.

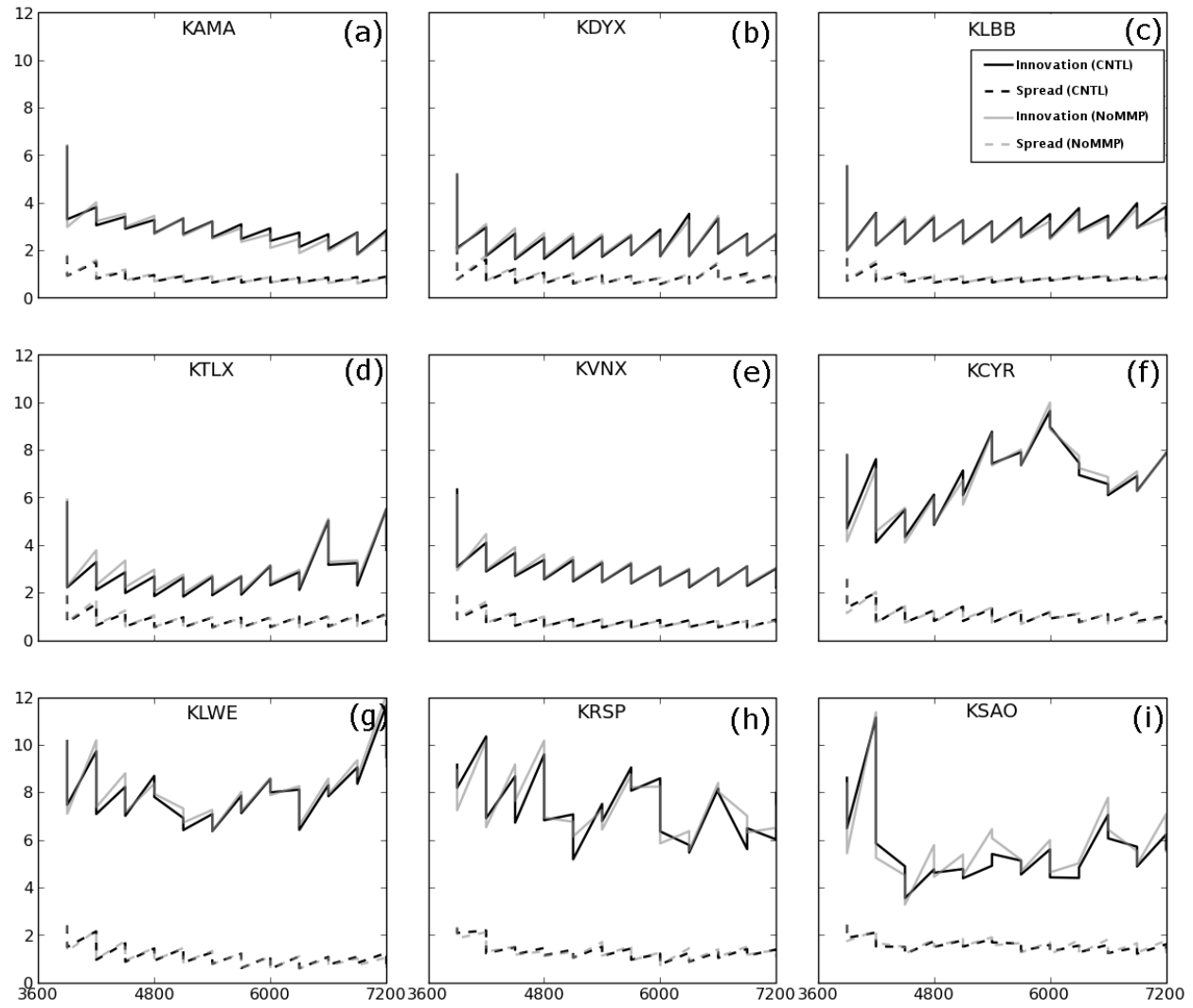


Fig. 13. As Fig. 10, but for experiments CNTL (black lines) and NoMMP (gray lines) including WSR-88D radars KAMA, KDYX, and KLBB and performing calculations over the entire model domain.

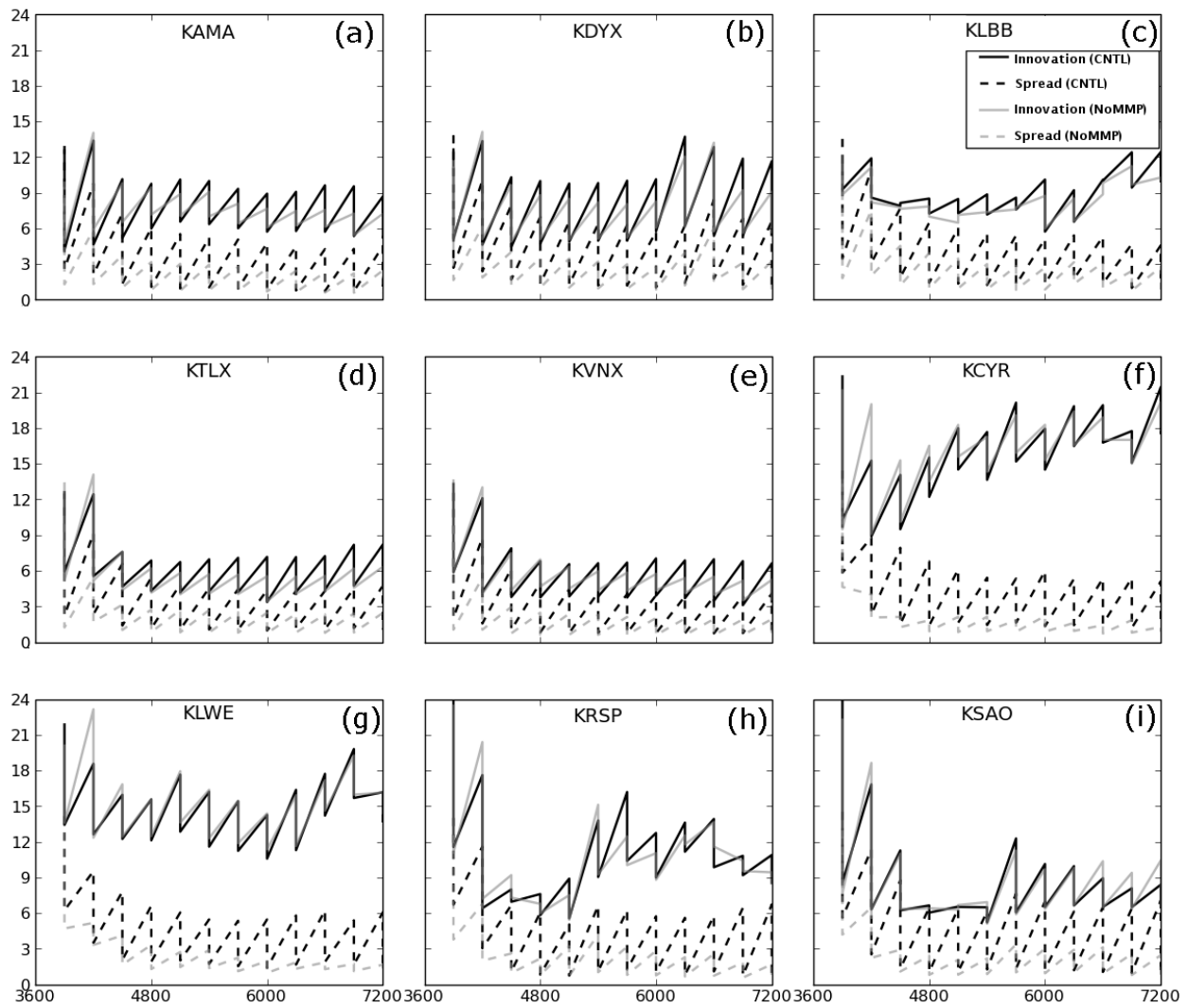


Fig. 14. As Fig. 11, but for radar reflectivity (in dBZ) instead of radial velocity.

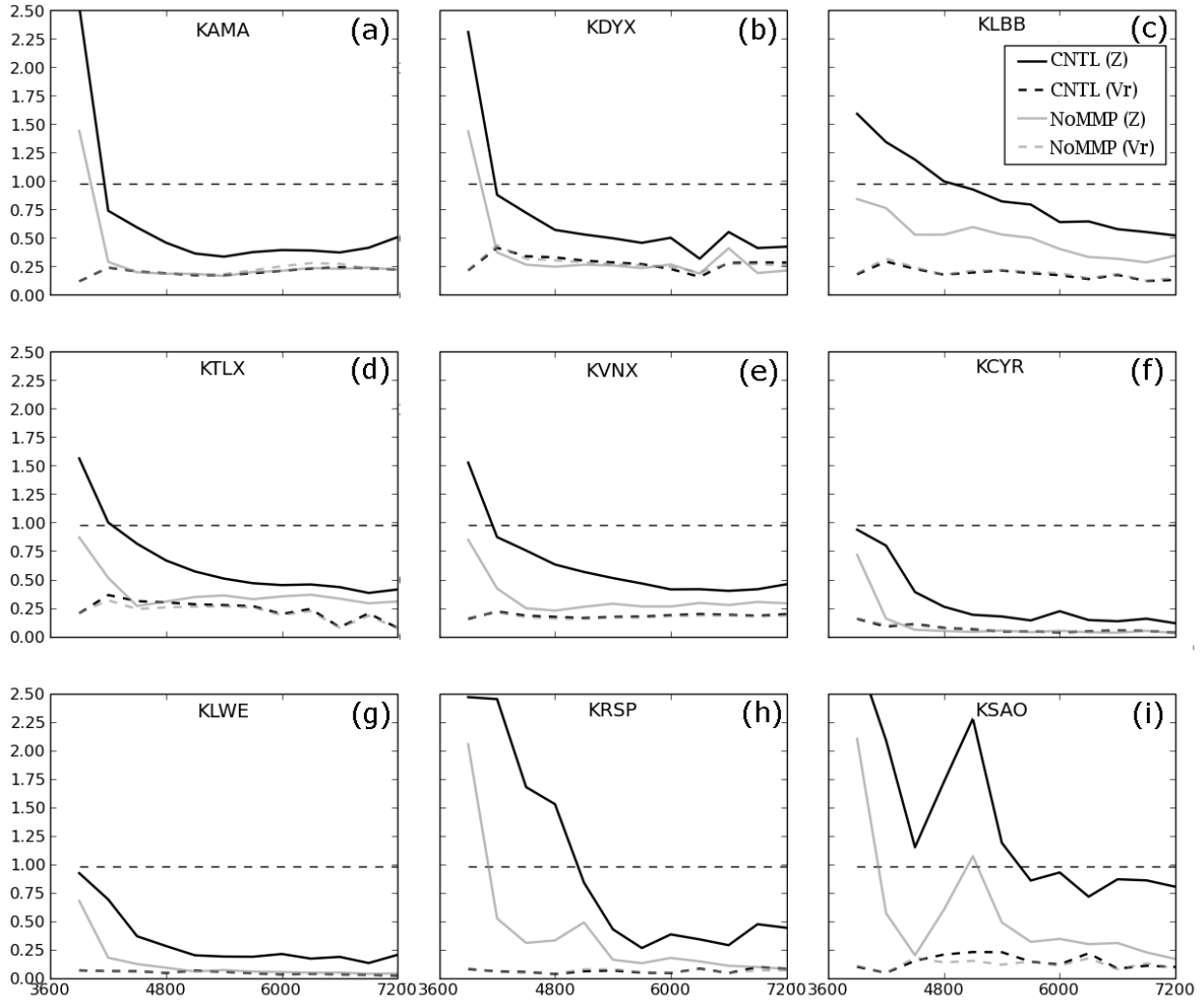


Fig. 15. As Fig. 12, but for experiments CNTL (black lines) and NoMMP (gray lines) including WSR-88D radars KAMA, KDXY, and KLBB and performing calculations over the entire model domain.

Table 1. Comparison of CASA X-band and WSR-88D S-band radar specifications

	<b>CASA</b>	<b>WSR-88D</b>
<b>Wavelength</b>	3.19 cm (X-band)	10.0 cm (S-band)
<b>Maximum Peak Power</b>	25 kW	750 kW
<b>Pulse Repetition Frequency</b>	Variable up to 3.33 kHZ	0.3 – 1.3 kHZ
<b>3 dB Beamwidth</b>	2.0 degrees	0.95 degrees
<b>Polarization</b>	Dual linear (V and H)	Single polarization (H only)
<b>Rotation Rate</b>	Variable up to 120 deg./s	36 deg./s
<b>Antenna Gain</b>	38 dB	45 dB
<b>Antenna Diameter</b>	1.5 m	8.5 m
<b>Maximum Range</b>	40 km	459 km

Table 2. Summary of experiments

	CNTL	NoCASA	NoMMP
<b>WSR-88D radar used?</b>	Yes	Yes	Yes
<b>CASA radar used?</b>	Yes	No	Yes
<b>Ensemble size</b>	40	40	40
<b>Number of Lin microphysics members</b>	16	16	40
<b>Number of WSM-6 microphysics members</b>	16	16	0
<b>Number of NEM microphysics members</b>	8	8	0

Table 3. List of radars used for data assimilation and their site locations and elevations.

<b>Radar Name</b>	<b>Radar Type</b>	<b>Latitude</b>	<b>Longitude</b>	<b>Elevation</b>
KAMA	WSR-88D	35.2333 N	101.7092 W	1113 m
KDYX	WSR-88D	32.5383 N	99.2544 W	357 m
KLBB	WSR-88D	33.6542 N	101.8142 W	1013 m
KTLX	WSR-88D	35.3331 N	97.2778 W	384 m
KVNX	WSR-88D	36.7408 N	98.1278 W	379 m
KCYR	CASA	34.8739 N	98.2522 W	448 m
KLWE	CASA	34.6239 N	98.2708 W	396 m
KRSP	CASA	34.8128 N	97.9306 W	436 m
KSAO	CASA	35.0314 N	97.9562 W	356 m